High-resolution convective wet scavenging simulations: A case study of the Fukushima Daiichi Nuclear Power Plant accident

Nuohang Liu[1,2], Baozhu Ge[1,2], Xingtao Su[3], Xueshun Chen[1,2], Oliver Wild[4], Yuanchun Zhang[2,5], Zhe Wang[1,2], Zifa Wang[1,2]

[1] State Key Laboratory of Atmospheric Boundary Layer Physics and Atmospheric Chemistry, Institute of Atmospheric Physics, Chinese Academy of Sciences, Beijing 100029, China

[2] University of Chinese Academy of Sciences, Beijing 100049, China

[3] Beijing Institute of Applied Meteorology, Beijing 100029, China

[4] Lancaster Environment Centre, Lancaster University, Lancaster LA1 4YQ, United Kingdom

[5] Key Laboratory of Cloud-Precipitation Physics and Severe Storms, Institute of Atmospheric Physics, Chinese Academy of Sciences, Beijing 100029, China

Correspondence author: Baozhu Ge (gebz@mail.iap.ac.cn)

Key Points:

- The ^{137}Cs deposition of Tokyo Metropolitan Area (TMA) is enhanced due to subgrid convective transport.
- The plume is dominated by fine-mode particles during plume 9 (March 21) at the TMA.
- A 20-min rather than 1-h meteorological field can represent the evolution of convective clouds in the weather front during plume 9.

Abstract

Convective precipitation is a key factor for diagnosing convective clouds and the subsequent modeling the wet scavenging of air pollutants in offline chemical transport models (CTMs). However, a discrepancy exists between the Weather Research and Forecasting model, which uses resolved convection, and CTMs, which rely on a diagnostic convective cloud scheme, in handling high-resolution convective wet scavenging simulations. To explore the uncertainties arising from this disparity, this study focuses on ^{137}Cs, released during the Fukushima Daiichi Nuclear Power Plant accident, as a species with numerous observations compared to other radionuclides and minimal interference from other factors using the NAQPMS model incorporating a physically-based wet deposition module. A diagnostic convective cloud scheme was applied, using a radar composite reflectivity factor (RCRF) of 35 dBZ to identify convective precipitation. Implementing the RCRF diagnosis scheme significantly improved model performance by increasing in-cloud deposition. This enhancement led to a 46%–48% increase in total deposition in the Tokyo Metropolitan Area. The results showed that dynamic conditions critically influence wet scavenging and that replenishment of convective transport is necessary to simulate high-resolution convective wet scavenging using offline CTMs.

Plain Language Summary

The current kilometer resolution is insufficient for high-resolution convective wet scavenging simulations, especially for offline chemical transport models (CTMs). To solve the problem, we chose ^{137}Cs released during Fukushima Daiichi Nuclear Power Plant accident as a stable indicator, and identified the convective precipitation as the input of the diagnostic convective cloud scheme of Nested Air Quality Prediction Modeling System (NAQPMS) model to activate the subgrid convective transport. The results show that the deposition of Tokyo Metropolitan Area where the plume accompanied with convective precipitation is enhanced, improving the model performance on deposition. The approach proposed in this study can make good use of offline CTMs in simulating high-resolution convective wet scavenging.

1 Introduction

The total precipitation predicted by both global climate models and mesoscale meteorological models like the Weather Research and Forecasting (WRF) model includes two main components: grid-scale precipitation and subgrid precipitation. Grid-scale precipitation is directly resolved by a microphysics scheme and represents precipitation that occurs on scales larger than the model grid, while the subgrid precipitation is parameterized using a cumulus parameterization scheme and represents precipitation that occurs on scales smaller than the model grid (Ahn and Kang, 2018; Skamarock et al., 2019). There are several schemes for characterizing cumulus convection in WRF, e.g., the Kain-Fritsch Eta scheme (Kain, 2004) which employ simple cloud model with moist updrafts and downdrafts, with the effects of detrainment, entrainment, and relatively simple microphysics (Skamarock et al., 2019), and the Grell 3D cumulus parameterization scheme which enables the distribution of subsidence effects to adjacent grid columns (Skamarock et al., 2019). When the model grid resolution is sufficiently fine (typically no greater than 4 km), cumulus parameterization schemes become unnecessary as the models can represent convection explicitly (i.e., explicit convection) (Dong et al., 2022; Gevorgyan, 2018; Lu et al., 2021; Prein et al., 2015; Weisman et al., 1997; Yu et al., 2025). However, previous studies reported that explicit convection and cumulus parameterized convection simulations could cause differences in precipitation intensity and frequency, this may due to the different convective available potential energy thresholds for triggering convection, resulting in frequent but weak convection or strong but low-frequency convection that affects heavy precipitation occurring and large-scale water vapor condensation (Argüeso et al., 2020; Zhang et al., 2021). For example, Wu et al. (2023) found that the Kain–Fritsch Eta cumulus parameterization scheme substantially increased total precipitation during a heavy precipitation event compared to explicit convection, due to large contribution of convective precipitation in the central rain area. In summary, the production of grid-scale and subgrid precipitation, influenced by model spatial resolution and parameterization schemes, is essential for accurate precipitation prediction and their role on aerosol scavenging (Feng et al., 2023; Wang et al., 2021; Xia et al., 2022).

In high-resolution convective wet scavenging simulations, online-coupled models such as WRF-Chem have inherent advantages due to the simultaneous calculation of meteorological and chemical processes during explicit convection, and the chemical module which coupled in the meteorological model can fully exploit the temporal and spatial resolution of the meteorological fields (Grell et al., 2005; Hu et al., 2014). Nevertheless, due to large uncertainties in explicit convection simulations, wet deposition is still underestimated even when secondary activation of aerosols was taken into account in high-resolution wet scavenging simulations using WRF-Chem (Yang et al., 2015). However, in most of the offline regional chemical transport models (CTMs), such as Nested Air Quality Prediction Modeling System (NAQPMS), third-Generation Community Multiscale Air Quality Modeling System (CMAQ), and Comprehensive Air quality Model with extensions (CAMx), convective wet scavenging is conducted by diagnostic convective cloud schemes that include aqueous chemistry, wet scavenging, and subgrid convective transport. The scheme in CMAQ handles precipitating clouds and non-precipitating clouds and NAQPMS chooses the similar strategy with CMAQ, while CAMx uses the Cloud-in-Grid scheme for simulating convective clouds, especially for subgrid convective transport (Emery et al., 2024; Ge et al., 2014; Roselle and Binkowski, 1999). But if the meteorological model employs explicit convection, these offline CTMs will switch off the diagnostic convective cloud schemes. Furthermore, their meteorological fields need to be spatial and temporal interpolated before the simulations, thus a large amount of information related to convective transport and convective evolution is lost. These limitations are detrimental to high-resolution convective wet scavenging simulations. In brief, the most important issue is that the current kilometer resolution is still insufficient to resolve cloud convection, the modeling of convective wet scavenging has high uncertainty. More importantly, we cannot adjust the modeling framework of these offline CTMs. Therefore, how to make good use of these offline CTMs in simulating high-resolution convective wet scavenging, subgrid convective transport should be considered as a workaround.

We adopted an offline CTM, NAQPMS model, for investigation in this study. ^{137}Cs mainly released in particulate form during the Fukushima Daiichi Nuclear Power Plant (FDNPP) accident was used as an indicator to investigate the effects of subgrid convective transport on particle wet scavenging due to its stability, long half-life and more observational data than other radionuclides (Mathieu et al., 2018; Zhuang et al., 2024). Although numerous studies have been conducted on the FDNPP accident, significant uncertainties persist in wet deposition modeling, demanding further investigation (Fang et al., 2022; Kajino et al., 2018). Fang et al. (2022) and Zhuang et al. (2023) demonstrated that different in-cloud and below-cloud scavenging schemes substantially impact deposition simulation results. Previous studies focusing on the FDNPP accident predominantly employed empirical formulations to estimate wet scavenging coefficients (Fang et al., 2022; Groëll et al., 2014; Hu et al., 2014; Leadbetter et al., 2015; Saito et al., 2015; Zhuang et al., 2023), rather than utilizing physically-derived equations critical for mechanistic interpretation of wet deposition processes. The NAQPMS model can avoid the problem, because it couples a physically modelled wet deposition module. Convective precipitation was independently identified using the radar composite reflectivity factor (RCRF) calculated from the meteorological field and used as the trigger of the diagnostic convective cloud scheme to avoid the. To simplified the discussion, two particle size bins representing the range of typical particle diameters were adopted to investigate the convective wet scavenging of different sizes of ^{137}Cs particles. The model performance in simulating convective clouds under varying temporal resolution was also discussed. The approach and findings of this study could help to conduct high-resolution convective wet scavenging simulations not only by NAQPMS, but also by other offline CTMs.

2 Methodology

2.1 Model introduction

NAQPMS is a three-dimensional offline Eulerian CTM developed by the Institute of Atmospheric Physics, Chinese Academy of Sciences. Advection is simulated by an accurate mass-conservation algorithm (Walcek and Aleksic, 1998). Gas-phase chemistry is represented using the "carbon bonding mechanism Z" (Zaveri and Peters, 1999). For inorganic aerosols, the ISORROPIA thermodynamic equilibrium module (Nenes et al., 1998) is used to simulate the ammonia–nitrate–sulfate–chloride–sodium–water system. A bulk yield scheme for secondary organic aerosols (SOAs), treated as six SOA species, is used in NAQPMS (Odum et al., 1997). The dry deposition of gases and aerosols is simulated using the Wesely (1989) scheme. Wet deposition and aqueous-phase chemistry are modeled using the CAMx and Regional Acid Deposition Model 2 (RADM2) mechanism, respectively (Wang et al., 2001). More details about the model can be found in Li et al. (2012).

To simulate the atmospheric behavior of ^{137}Cs during the FDNPP accident, a new variant of the NAQPMS model was developed. Within this model, chemical reactions are not considered. The emissions module specifics the location, release timing, and emission rates for each point source, and aligns the update interval of emission data with the model integration timestep to reduce uncertainty. Following Hu et al. (2014), the decay module considers radioactive decay as a first-order loss rate. The dry deposition of gaseous and particulate radionuclides is simulated using the Zhang et al. (2003) and Zhang et al. (2001) schemes, respectively.

Wet deposition module was modeled following Ge et al. (2014) and Xu et al. (2019). The module includes a diagnostic convective cloud scheme and a grid scale cloud scheme. The grid scale cloud scheme processes resolved cloud occupying the entire grid cell, and the cloud lifetime (e.g. the scheme's timestep) is synchronized to model integration steps. In the contrast, the diagnostic convective cloud scheme assumes that the ascending air parcel occupies the area smaller than the grid cell and assumes 1 hour cloud lifetime (e.g. the scheme's timestep as well). Subgrid convective transport algorithm inherits the Regional Acid Deposition Model (RADM) framework (Chang et al., 1987). Pollutant concentrations in convective clouds $\overline{\mathrm{m}}_{\mathrm{i}}^{\mathrm{cld}}(\mathrm{z})$ is calculated as:

$$\overline{m}_i^{cld}(z) = f_{ent}\left[(1 - f_{side})\overline{m}_i^{down} + f_{side}\overline{m}_i(z)\right] + (1 - f_{ent})\overline{m}_i^{up} \tag{1}$$

where f_{side} denotes the fraction of entraining air originating from the side of the cloud, the entrainment ratio f_{ent} is determined through iterative solution of mass-energy conservation equations, $\overline{m}_i^{down}$ and $\overline{m}_i^{up}$ represent pollutant concentrations above cloud top and cloud base, respectively. $\overline{m}_i(z)$ is the pollutant concentration of the layer z. Pollutant concentrations and meteorological variables are vertically averaged, before calculations of wet scavenging and wet deposition.

Wet scavenging of the two schemes includes in-cloud and below-cloud scavenging. The in-cloud scavenging assumes complete removal of accumulation and coarse mode particles by cloud water, the in-cloud scavenging coefficient is defined as the reciprocal of cloud water removal timescale. The below-cloud scavenging of particles is considered irreversible, primarily influenced by precipitation intensity, collection efficiency, and particle size. The collection efficiency has six mechanisms: Brownian diffusion, directional interception, inertial impaction, thermophoresis, diffusiophoresis, and electrostatic interaction, effectively improving underestimation of below-cloud scavenging coefficients in the Greenfield gap size range (Xu, 2020).

2.2 Model configuration

The simulations were performed using two nested domains (Figure 1a). Domain 1 covers most of the Japanese islands on a Lambert conformal map projection with 197×207 grid cells at a 9-km horizontal resolution, while Domain 2 focuses on the

Kanto region and the Tohoku region with 252×276 grid cells at a 3-km horizontal resolution. The simulations used 32 terrain-following layers from the surface to 31 km altitude. Under the configuration, 6~7 vertical layers were allocated below 1 km, the thickness of the lowest layer was about 80~90 m. A part of the model vertical layers was allocated in the stratosphere, due to that the deep convective cloud tops can penetrate into the lower stratosphere (Dessler, 2009; Rossow and Pearl, 2007). However, the vertical layers contained about 24 layers below 15 km, suggesting that most of the modeled vertical layers were located in the troposphere, it was finer than the previous NAQPMS configuration with 20 terrain-following layers extending from the surface to 20 km a.s.l. (Ge et al., 2014; Tan et al., 2023). The location of FDNPP (37.42°N, 141.03°E; shown in Figure 1a and 1b as a red star) was used to determine the location of point source in both domains. The integration timesteps for Domain 1 and Domain 2 were 600 and 300 s, respectively. The emissions inventory of ^{137}Cs provided by Katata et al. (2015) was adopted, and all ^{137}Cs assumed to be in the particulate phase and water-soluble (Kajino et al., 2019). Simulations with a 1-h output interval were initiated from 05:00 March 12 (JST) and ended at 00:00 April 1 (JST) 2011, covering the period of principal ^{137}Cs releases.

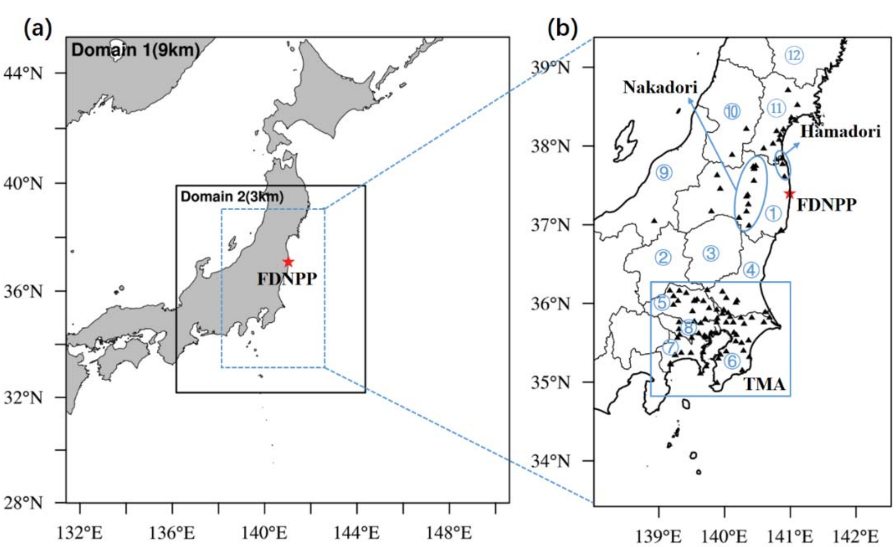

Figure 1. (a) Map of the two nested domains. (b) The observation site locations (black triangles); prefectures are numbered in blue: 1: Fukushima; 2: Gunma; 3: Tochigi; 4: Ibaraki; 5: Saitama; 6: Chiba; 7: Kanagawa; 8: Tokyo; 9:Nigata; 10:Yamagata; 11:Miyagi; 12: Iwate

The meteorological fields for NAQPMS were simulated by the WRF model, version 4.0 (Skamarock et al., 2019). with a 20-min output interval for both domains, because according to the typical relationship between the time scale and spatial scale of atmospheric phenomena, 20-min temporal resolution is enough to represent atmospheric phenomena with 3-km spatial scale (Mölders and Kramm, 2014). ERA5 (the fifth-generation ECMWF reanalysis), with a 0.25° horizontal resolution and a three-hourly update, provided the initial and boundary conditions for the WRF model. The Single-Moment 6-class (WSM6) scheme (Hong and Lim, 2006) was adopted for the cloud microphysics in both domains. The Grell 3D cumulus parameterization scheme was only set in Domain 1, Domain 2 employed explicit convection.

2.3 Experimental setup

With cumulus parameterization schemes switched off in Domain 2, all WRF precipitation outputs of Domain 2 were produced as non-convective precipitation and no convective precipitation appeared. For Domain 2, after acquiring WRF meteorological outputs, the NCAR Command Language (NCL) function "wrf_user_getvar" was employed to compute Radar Composite Reflectivity Factor (RCRF) of grid cells for precipitation field identification. Given WRF's 20-min output interval, the computed RCRF maintained the same temporal resolution. A reflectivity factor value of 35 dBZ was chosen as the threshold for identifying convection, because RCRF values greater than this suggests convective weather (Abulimiti et al., 2023; Gallucci et al., 2020; Zhao et al., 2024). For grid cells with RCRF values exceeding 35 dBZ, their convective precipitation amounts were assigned with the same values of non-precipitation amounts, while their original non-convective precipitation amounts were reset to zero. When their RCRF values were below 35 dBZ, non-convective precipitation amounts were retained and convective precipitation amounts were kept zero. Consequently, the total precipitation quantity remained conserved. The simulations used the identified precipitation are referred to the abbreviation of "CONV" . In CONV simulations, the diagnostic convective cloud scheme in NAQPMS models first determines whether convective precipitation is present at each grid cells. if so, the processes of subgrid convective transport, wet scavenging and wet deposition will be performed, otherwise the scheme will be skipped (hereafter, diagnostic convective cloud scheme that reads the precipitation identified using RCRF derived from WRF meteorological outputs is referred as RCRF diagnosis scheme). In contrast to the CONV simulation, new simulations were set up where the default non-convective precipitation is read directly by the NAQPMS model, referred to the abbreviation of "CTRL". In the CTRL simulations, the precipitation can only be read by the grid scale cloud scheme and perform wet scavenging and wet deposition without subgrid convective transport. Notably, this approach only changes the precipitation type, excluding significant impacts caused by changes in precipitation amount and frequency on wet deposition simulations (Wang et al., 2021; Xia et al., 2022).

Table 1 Summary of the simulations

Simulation	Use of RCRF	Proportion of coarse-mode particles	Proportion of fine-mode particles	Temporal resolution of meteorological field	Timestep of RCRF diagnosis scheme in Domain 2
CONV_00	Yes	0%	100%	20 minutes	5 minutes
CONV_03	Yes	3%	97%	20 minutes	5 minutes
CONV_10	Yes	10%	90%	20 minutes	5 minutes
CONV_20	Yes	20%	80%	20 minutes	5 minutes
CONV_30	Yes	30%	70%	20 minutes	5 minutes
CONV_40	Yes	40%	60%	20 minutes	5 minutes
CONV_50	Yes	50%	50%	20 minutes	5 minutes
CTRL_00	No	0%	100%	20 minutes	——
CTRL_03	No	3%	97%	20 minutes	——
CTRL_10	No	10%	90%	20 minutes	——
CTRL_20	No	20%	80%	20 minutes	——
CTRL_30	No	30%	70%	20 minutes	——
CTRL_40	No	40%	60%	20 minutes	——
CTRL_50	No	50%	50%	20 minutes	——
CONV_20min	Yes	0%	100%	20 minutes	20 minutes
CONV_1hr	Yes	0%	100%	1 hour	1 hour

Notes: "Fine-mode particles" denotes particles ranging from 0.1–2.5 μm and "Coarse-mode particles" denotes particles ranging from 2.5–10 μm.

Most ^{137}Cs particles are observed in diameter from 0.1 to 10 μm (Doi et al., 2013; Kaneyasu et al., 2012; Miyamoto et al., 2014), and this diameter range was used for the ^{137}Cs particles in the simulations across two size bins. A diameter of 2.5 μm served as the boundary to distinguish coarse-mode particles (2.5–10 μm) from fine-mode particles (0.1–2.5 μm). The activity median aerodynamic diameter of ^{137}Cs particles ranges from 0.5 to 2.0 μm, with a majority of particles below 2.5 μm in diameter observed (Doi et al., 2013; Kaneyasu et al., 2012; Miyamoto et al., 2014; Muramatsu et al., 2015), although a secondary peak at ~6 μm was also noted in the study of Miyamoto et al. (2014). Based on these works, under the assumption that the radioactivity proportion of coarse-mode particles is not greater than that of fine-mode particles, a dense setup of the proportion of coarse-mode particles, including 0%, 3%, 10%, 20%, 30%, 40%, and 50%, was employed in the simulations, while the remaining particles were allocated to the fine-mode particles.

The combination of two types of precipitation and seven particle size distribution generates 14 simulations labeled as X_Y, where X denotes either CONV or CTRL, and Y represents the proportion of coarse-mode particles. To investigate the impacts of the cloud lifetime in diagnostic convective cloud scheme and temporal resolution of meteorological fields, two additional simulations were implemented. The first simulation (CONV_1hr) used hourly meteorological inputs and the default cloud lifetime, which is typically applied to coarse spatial resolution simulations. However, the spatial resolution in Domain 2 is much finer, and thus the second simulation (CONV_20min) employed 20-min cloud lifetime aligned with the temporal resolution of meteorological fields. The CONV simulations adopted 5-min cloud lifetime to match model integration step and 20-min meteorological inputs, designed to investigate the effect of changes in cloud lifetimes on simulations. Details of all the simulations are provided in Table 1.

2.4 Observational data

The observational variables included precipitation rate, surface wind direction, and ^{137}Cs deposition and concentration. For precipitation rate, two datasets were employed: the modeled accumulated precipitation over land was validated using the 0.01°-gridded hourly precipitation dataset for Japan from Hatono et al. (2022), while maritime accumulated precipitation was validated using satellite-derived precipitation data from the Climate Prediction Center Morphing Technique (CMORPH) Climate Data Record, which has an 8-km spatial resolution and 30-min temporal resolution provided by the National Oceanic and Atmospheric Administration (NOAA) Climate Prediction Center (NOAA, 2024b). For surface wind direction, hourly records were obtained from Integrated Surface Dataset (NOAA, 2024a). For ^{137}Cs deposition, the cumulative ^{137}Cs deposition over land measured from aircraft (Fang et al., 2022) was used for analysis. Daily bulk (dry + wet) deposition observed with bulk samplers in each prefecture was also employed (Japanese Ministry of Education, Culture, Sports, Science and Technology, 2011). Hourly atmospheric ^{137}Cs concentration measurements from operational aerosol sampling at 99 sites (shown in Figure 1b as black triangles) in the national Suspended Particulate Matter (SPM) network of aerosols less than 10 μm in diameter (Oura et al., 2015) were used. Based on the observed ^{137}Cs concentrations from SPM sites, nine plumes that occurred during 12–23 March 2011 were identified (Tsuruta et al., 2014). Their details are shown in Table S1. Model intercomparison projects revealed that plumes 1, 5 and 6 observed approximately 30 km north of FDNPP are difficult to reproduce in 3-km resolution simulations, considering that models cannot effectively resolve atmospheric phenomena at spatial scales smaller than 6~10 times the model spatial resolution (Sato et al., 2018). They also revealed that plumes 4 and 7 are easily failed to reproduced due to their high sensitivities to spatiotemporal of wind field (Kitayama et al., 2018). Hence plumes 2, 3, 8, 9 can be relatively well reproduced by models (Fang et al., 2022; Kitayama et al., 2018; Sato et al., 2018; Zhuang et al., 2023), and were selected for validation in this study.

3 Results and discussion

3.1 Model validation

Validation of the simulations focused on the cumulative precipitation and ^{137}Cs deposition and concentration. The methods and statistical scores are detailed in the Text S1. Precipitation during the entire simulation period was validated against observed data over land and ocean, because there is a considerable quantity of invalid data over land in CMORPH, especially in mountainous areas. Figure S1 shows that WRF generally reproduces the spatial patterns of both land and ocean precipitation, but overestimates the magnitude, particularly in the mountainous regions of western Japan and over the ocean southeast of Japan.

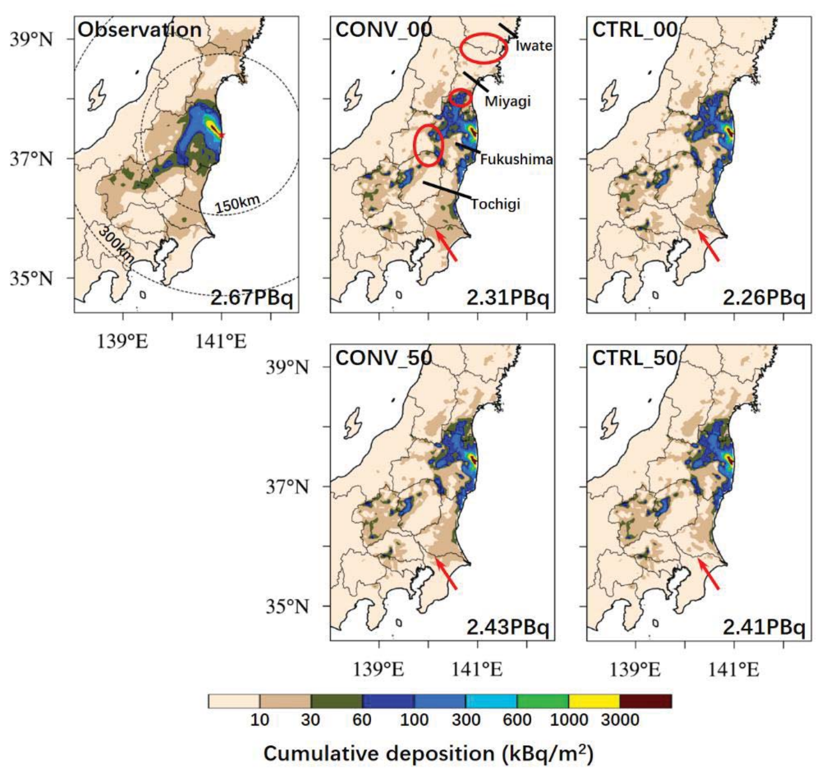

Figure 2. Cumulative ^{137}Cs deposition patterns over land from the observations and from CONV_00, CTRL_00, CONV_00, and CTRL_50 simulations. Red arrows indicate the TMA area, in which the deposition patterns are different between the simulations, cumulative ^{137}Cs deposition amount over land are shown in the lower right corner of the figures.

The model generally reproduced the concentrations during Plume 2, 3, 8, 9 (see Figure S2). However, the simulations with a lower proportion of coarse-mode particles show good performance in representing ^{137}Cs concentrations, while higher proportions result in poorer performance (see Figure S3a). Moreover, CONV simulations are slightly better than the CTRL simulations with the same particle size distribution. Most simulations perform well for plumes 2, 3, and 8, but plume 9 is less accurately captured, with a few CONV simulations with lower proportion of coarse-mode particles performing well and all CTRL simulations performing poorly (see Figure S4). Convective wet scavenging and the particle size distribution also have effects on representing these plumes; for instance, increasing the proportion of coarse-mode particles worsens performance for plume 8, while CONV simulations consistently outperform CTRL simulations for plume 9.

Validation results for simulations of the cumulative deposition of ^{137}Cs over land are shown in Figure S3b, CONV simulations show good performance, but CTRL simulations do not perform well due to figure of merit in space (FMS) scores below 70 (FMS score characterizes the overlap of two deposition distributions). Through a comparison between the observed and simulated patterns of cumulative deposition of ^{137}Cs over land in CONV_00 (as shown in Figure 2; patterns for all 14 simulations over Domain 2 are shown in Figure S5), we find that the simulation underestimates cumulative deposition to the north of Miyagi and south of Iwate, as well west of Fukushima and north of Tochigi, but the cumulative deposition south of Miyagi is overestimated. These discrepancies are consistent across other simulations and result in total land deposition underestimations of 9%–15%.

Validation results of CONV_00, CONV_20min, and CONV_1hr are shown in Figure. S6 and S7. The results of CONV_00 and CONV_20min are similar and show good performance with respect to both the concentration and deposition. CONV_1hr performs well in concentrations with better scores for plumes 2, 3 and 8 than CONV_00 and CONV_20min, but performs worse for plume 9 (RANK2 < 1, the definition of RANK2 can be found in Text S1). However, CONV_1hr's results are poor in deposition (FMS < 70). Cumulative deposition patterns (Figure S8) show that

CONV_00 and CONV_20min are similar, but there is an overestimation in Chiba and underestimation in Gunma in CONV_1hr, and it shows a more underestimated deposition compared to CONV_00 and CONV_20min.

3.2 Overview of the simulations

The contributions of dry, in-cloud and below-cloud deposition of ^{137}Cs over land in the simulations are shown in Figure 3a. As can be seen, in-cloud deposition was predominant, while dry, below-cloud, and total deposition amounts increased with the proportion of coarse-mode particles. The proportion of below-cloud deposition in wet deposition ranged from 3.5% to 23.9% in this study, which is consistent with most of the simulations in Fang et al. (2022). As shown in Figure 3b, the wet deposition amounts in the CONV simulations were slightly higher than in the CTRL simulations under the same particle size distribution owing to the convective wet scavenging. Due to the more intensive cloud convection over ocean than land (shown in Figure S9), the wet deposition amounts in the CONV simulations increased significantly, by 43%–60% (Figure 3d).

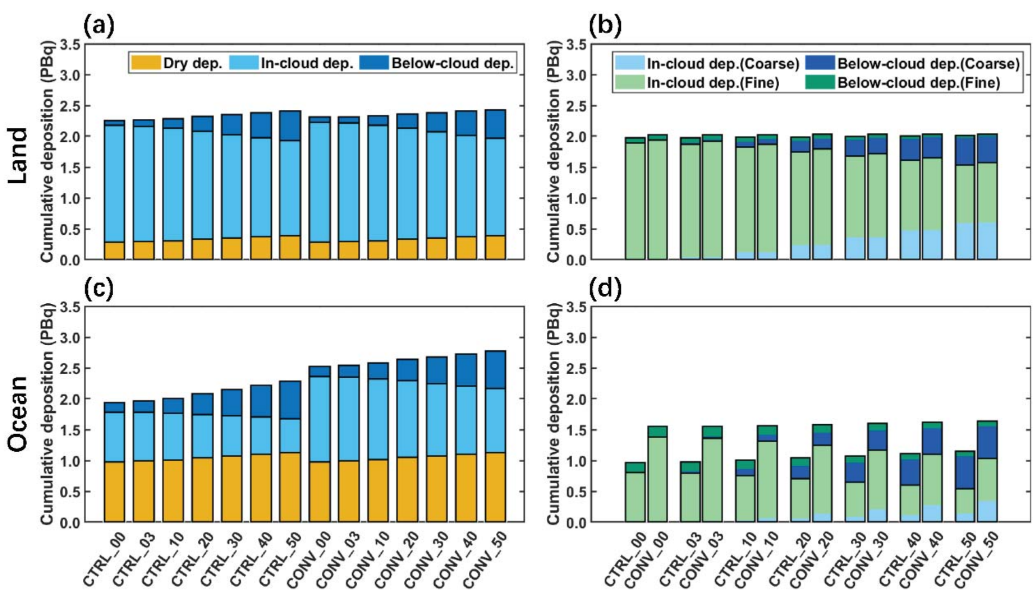

Figure 3. Comparison of (a, b) land and (c, d) ocean deposition amounts over the whole period.

The land deposition within various distances of FDNPP between the simulations and the observation are shown in Figure 4a. The model overestimates deposition within 10 km of FDNPP and show underestimation at 20–60km, leading to an underestimation of total land deposition, but the simulated deposition at 60–300 km is generally consistent with observations. Additionally, differences in the deposition amount due to convective wet scavenging mainly occurs at distances exceeding 150 km from FDNPP (see Figures 4b and 4c). In this area, the deposition estimated in the CONV simulations is significantly greater than that in the CTRL simulations, but the difference gradually declines with the proportion of coarse-mode particles. This aligns with the difference in the spatial deposition pattern in the Tokyo Metropolitan Area (TMA), which is also located more than 150 km south of FDNPP (indicated by the red arrows in Figure 2), where CONV simulations predict a larger area with cumulative deposition exceeding 10 kBq/m^2 than CTRL simulations.

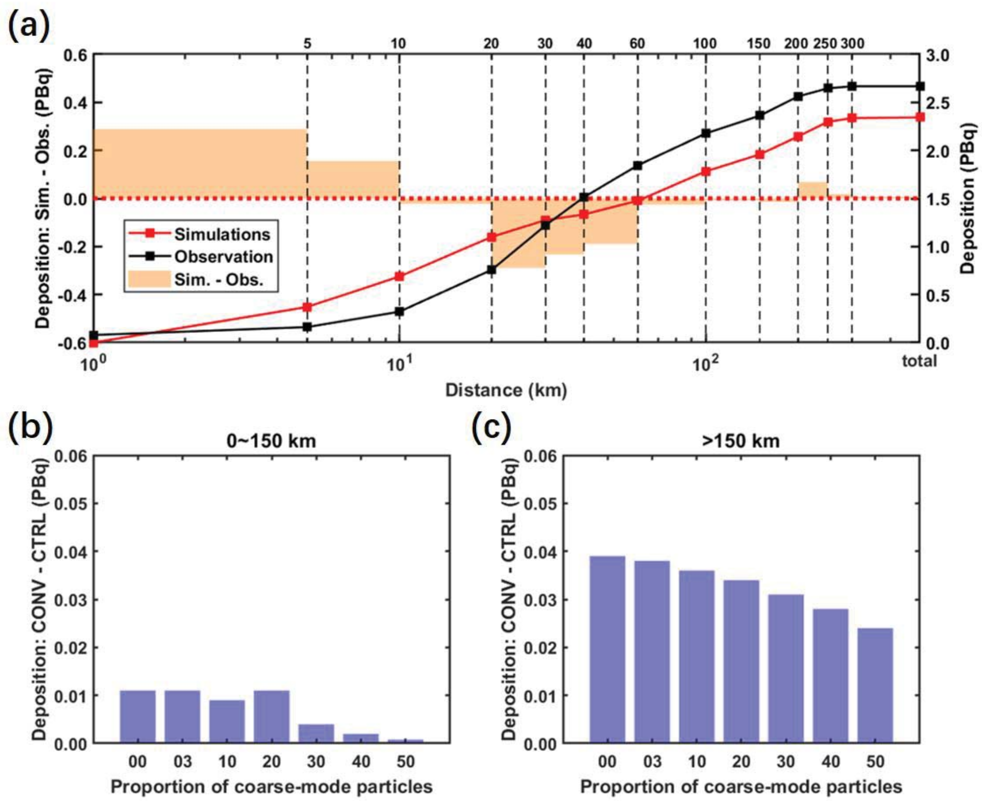

Figure 4. (a) The average of 14 simulations (red line) and the observation (black line) on land deposition amount within various distances of FDNPP and differences of them across the distance intervals, as well as the difference on land deposition between CONV and CTRL simulations with the same particle size distribution (b) within 150 km or (c) greater than 150 km from FDNPP. The distances of 150 and 300 km are shown by the black dashed rings in the upper-left panel of Figure 2.

The time sequences of ^{137}Cs emissions and cumulative land dry and wet deposition in CONV_00 are shown in Figure 5a. Significant deposition fluxes dominated by wet deposition occurred during three periods: March 15–16, March 20–21, and March 30–31, accounting for 66%–69%, 21%–22%, and 2%–3% of total deposition amount, respectively. This is similar to the results of standard-case (STD) simulation of Morino et al. (2013). After comparing time sequence of deposition shown in Figure

5a, 3-h precipitation time sequences of Nakadori and the TMA and time of occurrence of four plumes (see Figure 5b, 5c), it can be inferred that the deposition process on March 15–16 at Nakadori was produced by plume 3, and the deposition processes on March 20–21 at Nakadori and the TMA were produced by plumes 8 and 9, respectively. Wet scavenging not occurred in plume 2, because there was no precipitation in the TMA. Notably, WRF simulated precipitation during plume 8 that was not observed as well, affecting validation scores varied with the proportion of coarse-mode particles due to size-resolved below-cloud scavenging. The observed precipitation occurred at the end of plume 8 when the concentrations had dropped to a low level (see Figure S10 for details). Since deposition was controlled by non-convective precipitation during plumes 3 and 8, the following discussion focuses on plume 9, which affected in the TMA on March 21.

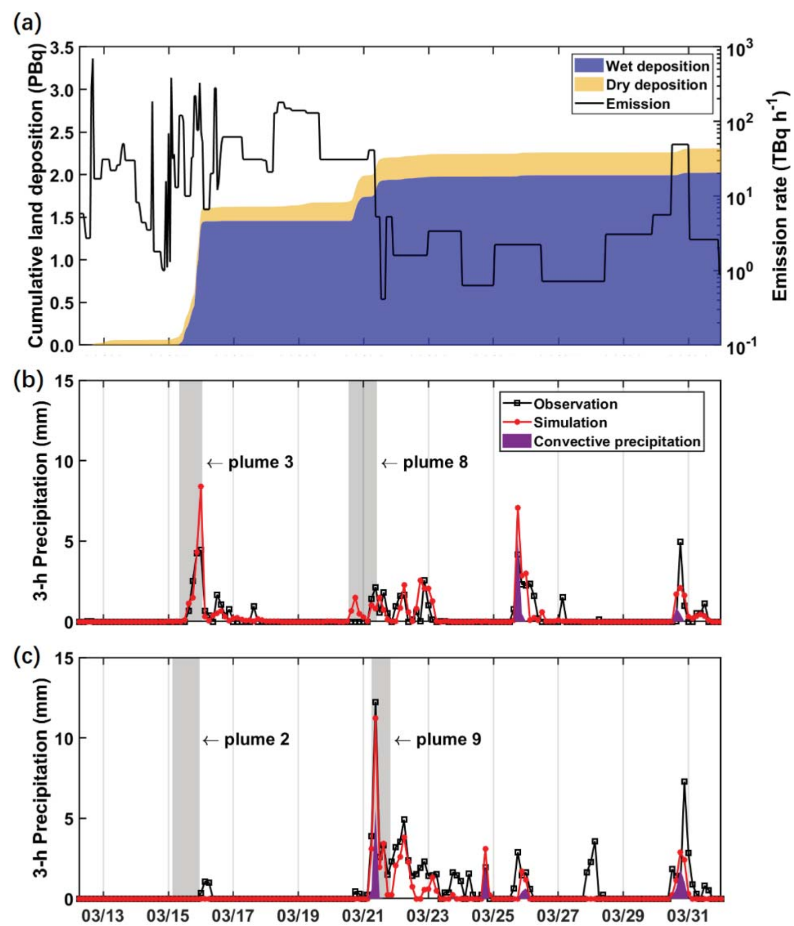

Figure 5. (a) Time sequence of emissions and cumulative land dry and wet deposition in CONV_00 during the entire simulation period, as long with the 3-h observed and simulated precipitation and identified convective precipitation for (b) Nakadori sites and (c) TMA sites. The periods of plumes 2, 3, 8 and 9 are highlighted in gray.

3.3 Convective process in plume 9

Taking CONV_00 as an example, the simulated plume followed a southern route from FDNPP through Fukushima, Ibaraki, and Chiba, influenced by precipitation during plume 9 (see Figure 6). However, the model underestimated the concentration and delayed the plume's arrival at the Tokyo Metropolitan Area (TMA) by 1–2 h. The wider simulated plume leads to overestimated concentrations at some sites in Chiba during 10:00–11:00. The weather front reported by Nakajima et al. (2017) was reproduced, as shown in Figures 7a and 7b. It resulted in the RCRF values calculated from the meteorological field being greater than 35 dBZ, and it was identified that there was a convective precipitation band with a similar route to the plume (shown in first column in Figure 8). The observed shift in wind direction at TMA sites, from southwesterly to northeasterly, was captured by the model but lagged by 1–2 h (see Figure S11), suggesting the plume trailed the weather front.

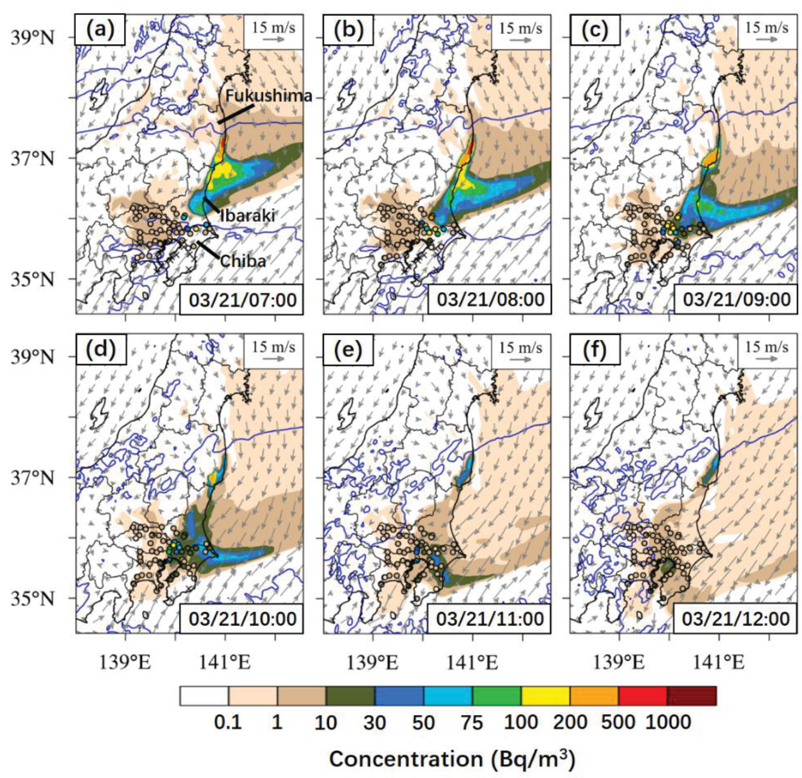

Figure 6. The simulated wind field and plume spread, along with the locations of observation sites in the TMA and their measurement of concentrations, during 07:00–12:00 on March 21 (the period of plume 9). Areas of simulated rainfall are outlined by blue lines.

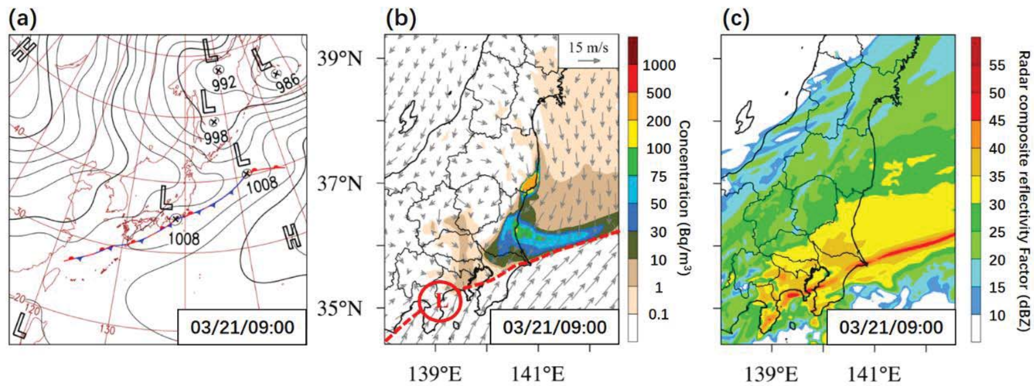

Figure 7. (a) Weather map for 09:00 on March 21 based on the Japan Meteorological Agency (JMA) analysis. (b) Location of the simulated weather front (red dashed line) and low-pressure system center (red "L") along with the simulated concentration and wind field. (c) Pattern of radar composite reflectivity calculated based on the meteorological field at 09:00 hrs.

Next, we take CONV_00 and CTRL_00 for comparison in the following discussion. As shown in Figure 8, there was no convective precipitation when the plume was transported southward at 07:00, hence there are no differences in the concentration vertical profiles and deposition patterns of CONV_00 and CTRL_00. At 08:00, convective precipitation began affecting the plume over Ibaraki and the adjacent sea. In CONV_00, subgrid convective transport caused a noticeable uplift of ^{137}Cs at the plume's leading edge, with concentrations exceeding 1 Bq/m^3 transported by updrafts to altitudes above 1 km, higher than that in CTRL_00. The differences in deposition between CONV_00 and CTRL_00 shows that subgrid convective transport formed polluted air masses with higher concentrations at surface, while lower concentrations appeared in the remaining areas. More high concentrations observed at TMA sites were captured than in CTRL_00, improving validation scores, because stronger vertical dynamic conditions in the CONV_00 led to more ^{137}Cs particles transported to the TMA. The effects of subgrid convective transport also emerge during the next period of 09:00–11:00. At 12:00, the plume was largely outside the convective precipitation band. Furthermore, it is noteworthy that these characteristics also appeared in other simulations with a greater proportion of coarse-mode particles.

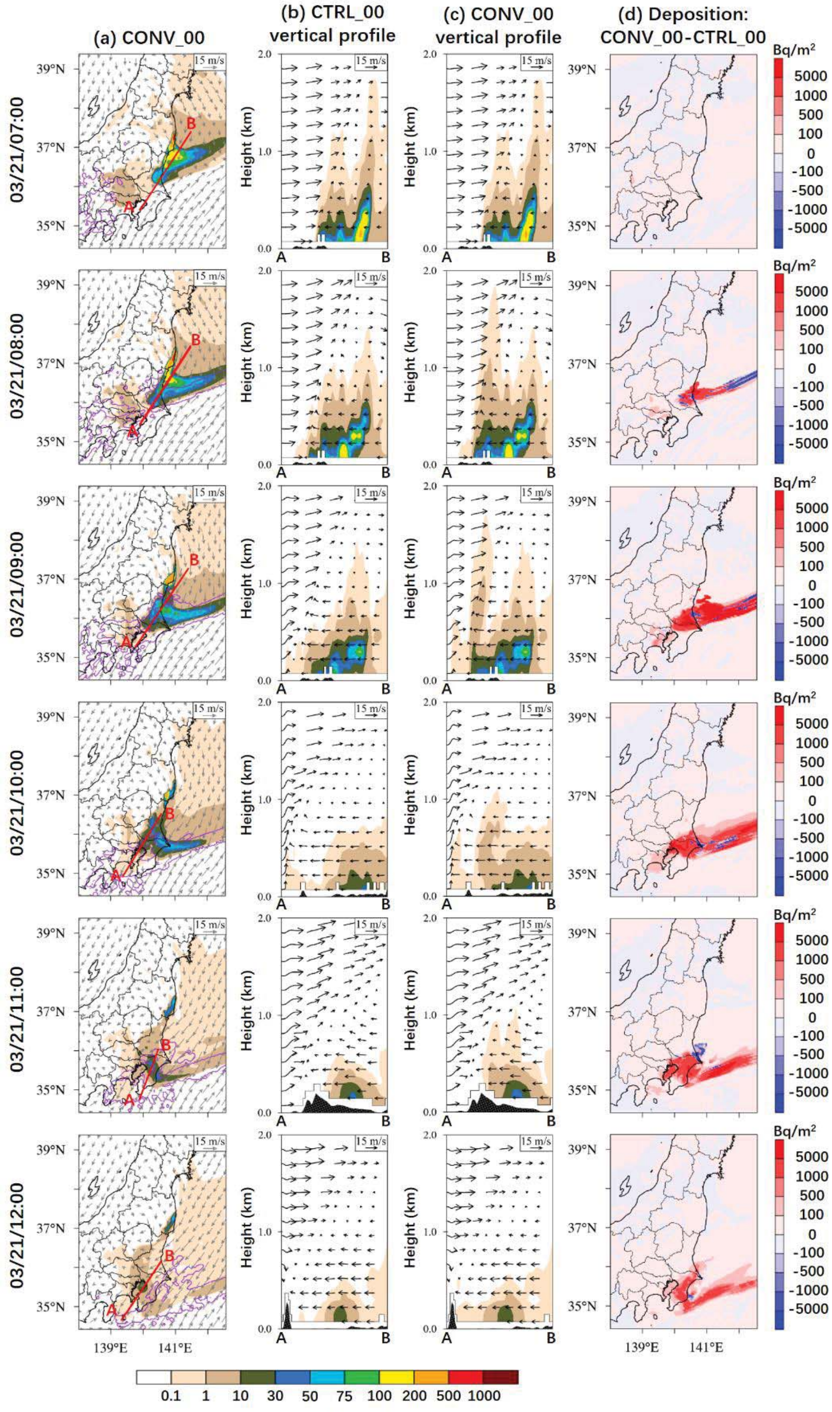

Figure 8. (a) Hourly simulated plume and wind field overlayed with the convective precipitation band (purple contours) during 07:00~12:00 on March 21. The red lines (A-B) denote the location of the vertical cross section for each hour. (b, c) Comparison of vertical profiles of the plume simulated by CONV_00 and CTRL_00. (d) Patterns of the difference in hourly deposition between CONV_00 and CTRL_00.

The cumulative convective precipitation pattern shows the footprint of the weather front during plume 9 (see Figure S12a). Gaps in the hourly precipitation field indicate insufficient temporal resolution for capturing the motion of the weather front, leading to incomplete scavenging and a larger plume-affected area at 12:00 (see Figure S12e), which allowed it to produce high-density deposition in central Chiba and overestimate ^{137}Cs concentrations in the TMA. By contrast, the 20-min convective precipitation field (see Figure S12b) offered more details, reducing gaps and enabling more extensive scavenging. This led to a smaller affected area and concentrated deposition in Ibaraki and northern Chiba (see Figure S12f). By comparing the validation results of concentration and deposition at plume 9 and TMA deposition pattern of CONV_00, CONV_20min and CONV_1hr, it can be found that mismatches between cloud lifetime and meteorological temporal resolution have insignificant impacts on simulated concentrations and deposition. However, the hourly meteorological inputs and the default cloud lifetime inadequately reproduce observed concentrations and deposition during the weather front event. Consequently, this case demonstrates that the configuration of hourly meteorological inputs and default cloud lifetime fails to represent motion of the weather front system in high-resolution simulation, at least 20-min meteorological inputs and cloud lifetime are needed.

3.4 Wet scavenging and deposition in plume 9

The average spatial distributions of the in-cloud and below-cloud scavenging coefficients of the two modes of particles in the CONV and CTRL simulations during plume 9 are shown in Figure 9. The in-cloud scavenging coefficients are not size-resolved, thus the values for both mode particles are identical. The enhancement of the in-cloud scavenging coefficients is not obvious, since the two mode particles belongs to accumulation or coarse mode particles which are assumed to be absorbed and scavenged by cloud water completely in the model regardless of the subgrid convective transport, but it is significant in the below-cloud scavenging coefficients due to the improved collision efficiency between rain droplets and ^{137}Cs particles via the subgrid convective transport. In addition, ^{137}Cs particles were uplifted to high elevations and easily captured by cloud droplets, increasing the ^{137}Cs concentration in cloud droplets and contributing to the in-cloud deposition (Tan et al., 2023). For fine-mode particles, in-cloud scavenging coefficients were greater than below-cloud scavenging coefficients (shown in Figure 9b), with more uplifted ^{137}Cs particles scavenged in the cloud than below the cloud, contributing to the rise of in-cloud deposition. Below-cloud scavenging coefficients also increase, contributing to higher below-cloud deposition. (shown in Table 2 and Figures 9a and 9b). For coarse-mode particles, the influence of subgrid convective transport similarly increases both in-cloud and below-cloud deposition, although their higher scavenging coefficients below-cloud than in-cloud (shown in Table 2 and Figures 9a and 9c). The rising in-cloud deposition of fine-mode particles provided the main contribution to the increase in the total deposition amounts in the CONV simulations by 46%–48% in the TMA during plume 9.

When compared to daily observed deposition averaged over the four TMA sites on March 21 shown in Figure S13, covering most period of plume 9, deposition in the CONV simulations is significantly higher than that in the CTRL simulations, with CONV_00 capturing the daily deposition well. However, underestimation progressively worsens in both CONV and CTRL simulations as the proportion of coarse-mode particles increases. Combined with the concentration validation results of plume 9, it can be inferred that the plume was almost dominated by fine-mode particles, which is similar to Zhuang et al. (2024).

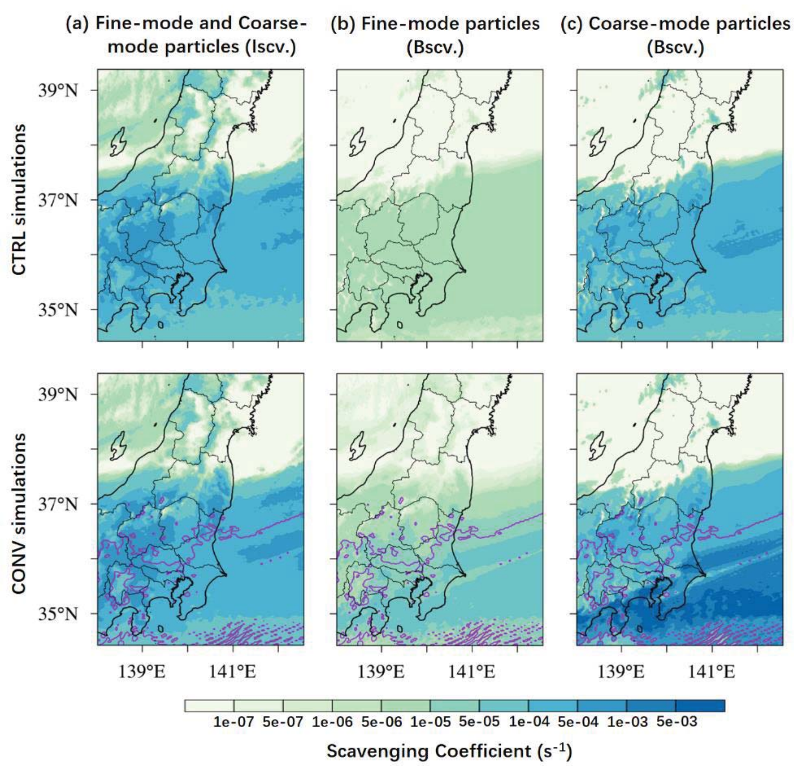

Figure 9. The distribution of (a) in-cloud scavenging coefficients of fine-mode and coarse-mode particles, and (b, c) below-cloud scavenging coefficients of (b) fine-mode particles and (c) coarse-mode particles in the CTRL simulations (first row) and CONV simulations (second row) during

plume 9. The areas where convective precipitation occurred during plume 9 are indicated by the purple contours in the figures of the CONV simulations.

In the CTRL simulations, the in-cloud scavenging coefficients of fine-mode particles were much higher than the below-cloud scavenging coefficients, and in-cloud deposition was responsible for 92.1% of wet deposition (see Table 2 and Figure 9). Nevertheless, for coarse-mode particles, the in-cloud scavenging coefficients were comparable to the below-cloud scavenging coefficients, and hence the contribution of in-cloud deposition was only 21.7%–22.8%. The subgrid convective transport uplifted the two modes of particles and also increased the below-cloud scavenging coefficients in the CONV simulations, thus there was a competition between in-cloud and below-cloud deposition. However, compared with fine-mode particles, the uplift effect has a stronger impact on coarse-mode particles, raising the in-cloud contribution from 21.7%–22.8% to 37.5%–39.1%.

Table 2 Statistics on cumulative land deposition in the TMA during plume 9

Simulation	Dry deposition (TBq)	Below-cloud deposition (TBq)		In-cloud deposition (TBq)		Total deposition (TBq)
		Fine-mode	Coarse-mode	Fine-mode	Coarse-mode	
CONV_00	3.25	7.39 (7.2%)	0.00	95.31 (92.8%)	0.00	105.94
CONV_03	3.25	7.16 (7.2%)	0.20 (62.5%)	92.45 (92.8%)	0.12 (37.5%)	103.17
CONV_10	2.94	6.65 (7.2%)	0.67 (61.5%)	85.77 (92.8%)	0.42 (38.5%)	96.47
CONV_20	3.25	5.91 (7.2%)	1.35 (61.1%)	76.24 (92.8%)	0.86 (38.9%)	87.61
CONV_30	2.34	5.17 (7.2%)	2.03 (61.0%)	66.70 (92.8%)	1.30 (39.0%)	77.55
CONV_40	2.05	4.43 (7.2%)	2.71 (60.9%)	57.17 (92.8%)	1.74 (39.1%)	68.10
CONV_50	1.76	3.69 (7.2%)	3.39 (60.9%)	47.63 (92.8%)	2.18 (39.1%)	58.66
CTRL_00	2.77	5.45 (7.9%)	0.00	63.54 (92.1%)	0.00	71.76
CTRL_03	2.71	5.29 (7.9%)	0.18 (78.3%)	61.64 (92.1%)	0.05 (21.7%)	69.87
CTRL_10	2.51	4.91 (7.9%)	0.61 (77.2%)	57.19 (92.1%)	0.18 (22.8%)	65.39
CTRL_20	2.27	4.36 (7.9%)	1.22 (77.2%)	50.83 (92.1%)	0.36 (22.8%)	59.04
CTRL_30	2.02	3.82 (7.9%)	1.83 (77.2%)	44.48 (92.1%)	0.54 (22.8%)	52.68
CTRL_40	1.76	3.27 (7.9%)	2.44 (77.5%)	38.13 (92.1%)	0.71 (22.5%)	46.31
CTRL_50	1.50	2.73 (7.9%)	3.05 (77.4%)	31.77 (92.1%)	0.89 (22.6%)	39.94

Note: The calculation region is the land part of the region outlined by the blue box denoted "TMA" shown in Figure 1. The percentages in parentheses represent the proportion of in-cloud deposition or below-cloud deposition relative to the wet deposition for fine-mode or coarse-mode particles, respectively.

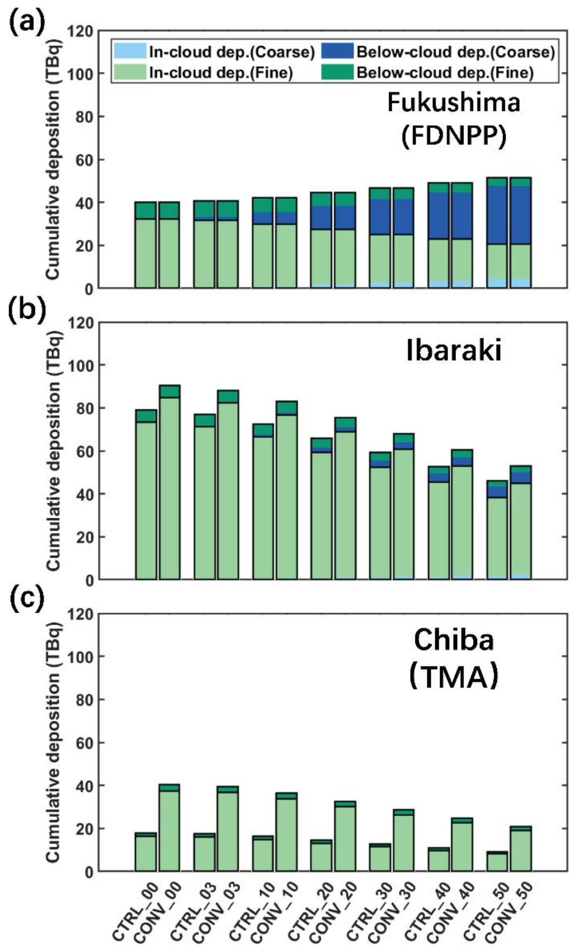

Figure 10. The cumulative deposition amount of in-cloud and below-cloud deposition of fine-mode and coarse-mode particles at (a) Fukushima, (b) Ibaraki, and (c) Chiba.

As shown in Figure 10, after the release of ^{137}Cs particles from FDNPP, coarse-mode particles in the plume were primarily deposited near Fukushima by below-cloud scavenging, and below-cloud deposition contributed roughly half of wet deposition in the simulations with a high proportion of coarse-mode particles (e.g. CTRL_50 and CONV_50). Since Fukushima is not significantly affected by convective precipitation, differences in wet deposition between CONV and CTRL simulations are minimal. When the plume was transported to Ibaraki, the wet deposition was dominated by in-cloud scavenging of fine-mode particles, while the contribution of coarse-mode particles had significantly declined. Convective precipitation noticeably enhanced wet deposition in the CONV simulations compared to the CTRL simulations with the same particle size distribution. When the plume was transported to Chiba, nearly all wet deposition was due to in-cloud scavenging of fine-mode particles, as coarse-mode particles were almost entirely absent. Convective wet scavenging remains active, similar to Ibaraki. In addition, wet deposition increased with the proportion of coarse-mode particles in Fukushima, but decreased in Ibaraki and Chiba. This was due to the fact that a large amount of coarse-mode particles had been scavenged at Fukushima when the residual plume dominated by fine-mode particles reached Ibaraki and Chiba with lower concentrations. Consequently, coarse-mode particles have shorter lifetimes and are predominantly deposited close to the source, while fine-mode particles are more likely to undergo convective wet scavenging. It also explains why the differences in deposition between the CONV and CTRL simulations decrease as the proportion of coarse-mode particles rises (see Table S2 and Figure 4c for details).

4 Conclusions

The release of particulate ^{137}Cs during the FDNPP accident was used in this study to investigate the process of convective wet scavenging in a high-resolution simulation of the NAQPMS model incorporating a physically modeled wet scavenging scheme. Convective precipitation was identified using RCRF values obtained from the input meteorological fields. The results showed that the disparity between WRF and NAQPMS in managing the high-resolution simulation of convective wet scavenging cause the underestimation of deposition. Considering the subgrid convective transport of ^{137}Cs during plume 9 would improve the performance of the CONV simulations. Due to subgrid convective transport, the ^{137}Cs particles were uplifted to a higher altitude and increased the amount and contribution of in-cloud deposition. This enhancement contributed to an increase in the total deposition amount in the TMA by 46%–48%, especially the contribution from the in-cloud deposition of fine-mode particles, since most coarse-mode particles were scavenged before they reached the TMA. The dynamic conditions are the critical factor affecting wet scavenging. In terms of the temporal resolution, a 20-min rather than 1-h meteorological field was found to be sufficient for accurate cloud convection simulations. This paper emphasis the importance of the synergistic consideration of dynamical processes between the physical factors and chemical substances during the convective transport simulations.

Acknowledgments

This work was funded by the National Natural Science Foundation of China (Grant 42122049). We thank Sheng Fang from Tsinghua University for supporting aircraft observed ^{137}Cs deposition.

Conflict of Interest

The authors declare that they have no conflicts of interest.

Open Research

The wind speed and direction data can be downloaded at NOAA (2024a). Two precipitation datasets can be found and downloaded at Hatono et al. (2022) and NOAA (2024b), respectively. The observed ^{137}Cs concentration can be found at Oura et al. (2015). The daily observed deposition at March 21 can be found at Japanese Ministry of Education, Culture, Sports, Science and Technology (2011). The aircraft observed ^{137}Cs deposition and the simulation results of this paper are available via Zenodo (Liu et al., 2024).

References

Abulimiti, A., Q. Sun, L. Yuan, Y. Q. Liu, J. Q. Yao, L. M. Yang, J. Ming, and A. Abulikemu (2023), A Case Study on the Convection Initiation Mechanisms over the Northern Edge of Tarim Basin, Xinjiang, Northwest China, *Remote Sens.*, *15*(19), 26, doi:10.3390/rs15194812.

Ahn, M.-S., and I.-S. Kang (2018), A practical approach to scale-adaptive deep convection in a GCM by controlling the cumulus base mass flux, *Npj Climate and Atmospheric Science*, *1*, doi:10.1038/s41612-018-0021-0.

Argüeso, D., R. Romero, and V. Homar (2020), Precipitation Features of the Maritime Continent in Parameterized and Explicit Convection Models, *J. Clim.*, *33*(6), 2449-2466, doi:10.1175/jcli-d-19-0416.1.

Chang, J. S., R. A. Brost, I. S. A. Isaksen, S. Madronich, P. Middleton, W. R. Stockwell, and C. J. Walcek (1987), A 3-dimensional eulerian acid deposition model - physical concepts and formulation, *J. Geophys. Res.-Atmos.*, *92*(D12), 14681-14700, doi:10.1029/JD092iD12p14681.

Dessler, A. E. (2009), Clouds and water vapor in the Northern Hemisphere summertime stratosphere, *J. Geophys. Res.-Atmos.*, *114*, 7, doi:10.1029/2009jd012075.

Doi, T., K. Masumoto, A. Toyoda, A. Tanaka, Y. Shibata, and K. Hirose (2013), Anthropogenic radionuclides in the atmosphere observed at Tsukuba: characteristics of the radionuclides derived from Fukushima, *J. Environ. Radioact.*, *122*, 55-62, doi:10.1016/j.jenvrad.2013.02.001.

Dong, G. T., Z. Y. Jiang, Y. Wang, Z. Tian, and J. G. Liu (2022), Evaluation of extreme precipitation in the Yangtze River Delta Region of China using a 1.5 km mesh convection-permitting regional climate model, *Clim. Dyn.*, *59*(7-8), 2257-2273, doi:10.1007/s00382-022-06208-1.

Emery, C. A., K. R. Baker, G. M. Wilson, and G. Yarwood (2024), Comprehensive Air Quality Model With Extensions, v7.20: Formulation and Evaluation for Ozone and Particulate Matter Over the US, *Geosci. Model Dev. Discuss.*, *2024*, 1-48, doi:10.5194/gmd-2024-48.

Fang, S., S. H. Zhuang, D. Goto, X. F. Hu, S. Li, and S. X. Huang (2022), Coupled modeling of in- and below-cloud wet deposition for atmospheric ^{137}Cs transport following the Fukushima Daiichi accident using WRF-Chem: A self-consistent evaluation of 25 scheme combinations, *Environ. Int.*, *158*, 16, doi:10.1016/j.envint.2021.106882.

Feng, J. W., C. Zhao, Q. Y. Du, M. Y. Xu, J. Gu, Z. Y. Hu, and Y. Chen (2023), Simulating Atmospheric Dust With a Global Variable-Resolution Model: Model Description and Impacts of Mesh Refinement, *Journal of Advances in Modeling Earth Systems*, *15*(10), 32, doi:10.1029/2023ms003636.

Gallucci, D., et al. (2020), Convective Initiation Proxies for Nowcasting Precipitation Severity Using the MSG-SEVIRI Rapid Scan, *Remote Sens.*, *12*(16), 18, doi:10.3390/rs12162562.

Ge, B. Z., Z. F. Wang, X. B. Xu, J. B. Wu, X. L. Yu, and J. Li (2014), Wet deposition of acidifying substances in different regions of China and the rest of East Asia: Modeling with updated NAQPMS, *Environ. Pollut.*, *187*, 10-21, doi:10.1016/j.envpol.2013.12.014.

Gevorgyan, A. (2018), Convection-Permitting Simulation of a Heavy Rainfall Event in Armenia Using the WRF Model, *J. Geophys. Res.-Atmos.*, *123*(19), 11008-11029, doi:10.1029/2017jd028247.

Grell, G. A., S. E. Peckham, R. Schmitz, S. A. McKeen, G. Frost, W. C. Skamarock, and B. Eder (2005), Fully coupled "online" chemistry within the WRF model, *Atmos. Environ.*, *39*(37), 6957-6975, doi:10.1016/j.atmosenv.2005.04.027.

Groëll, J., D. Quélo, and A. Mathieu (2014), Sensitivity analysis of the modelled deposition of ^{137}Cs on the Japanese land following the Fukushima accident, *Int. J. Environ. Pollut.*, *55*(1-4), 67-75, doi:10.1504/ijep.2014.065906.

Hatono, M., M. Kiguchi, K. Yoshimura, S. Kanae, K. Kuraji, and T. Oki (2022), Data for: A 0.01-degree gridded precipitation dataset for Japan, 1926-2020 [Dataset]. H. Dataverse, https://doi.org/10.7910/DVN/J215UY.

Hong, S.-Y., and J.-O. J. Lim (2006), The WRF single-moment 6-class microphysics scheme (WSM6), *Asia-Pacific Journal of Atmospheric Sciences*, *42*(2), 129-151.

Hu, X., D. Li, H. Huang, S. Shen, and E. Bou-Zeid (2014), Modeling and sensitivity analysis of transport and deposition of radionuclides from the Fukushima Dai-ichi accident, *Atmos. Chem. Phys.*, *14*(20), 11065-11092, doi:10.5194/acp-14-11065-2014.

Japanese Ministry of Education, Culture, Sports, Science and Technology (2011), Reading of radioactivity level in fallout by prefecture. https://radioactivity.nra.go.jp/en/results/land/prefecture/fallout?page=10.

Kain, J. S. (2004), The Kain-Fritsch convective parameterization: An update, *J. Appl. Meteorol.*, *43*(1), 170-181, doi:10.1175/1520-0450(2004)043<0170:Tkcpau>2.0.Co;2.

Kajino, M., T. T. Sekiyama, Y. Igarashi, G. Katata, M. Sawada, K. Adachi, Y. Zaizen, H. Tsuruta, and T. Nakajima (2019), Deposition and Dispersion of Radio-Cesium Released Due to the Fukushima Nuclear Accident: Sensitivity to Meteorological Models and Physical Modules, *J. Geophys. Res.-Atmos.*, *124*(3), 1823-1845, doi:10.1029/2018jd028998.

Kajino, M., et al. (2018), Lessons learned from atmospheric modeling studies after the Fukushima nuclear accident: Ensemble simulations, data assimilation, elemental process modeling, and inverse modeling, *Geochem. J.*, *52*(2), 85-101, doi:10.2343/geochemj.2.0503.

Kaneyasu, N., H. Ohashi, F. Suzuki, T. Okuda, and F. Ikemori (2012), Sulfate Aerosol as a Potential Transport Medium of Radiocesium from the Fukushima Nuclear Accident, *Environ. Sci. Technol.*, *46*(11), 5720-5726, doi:10.1021/es204667h.

Katata, G., et al. (2015), Detailed source term estimation of the atmospheric release for the Fukushima Daiichi Nuclear Power Station accident by coupling simulations of an atmospheric dispersion model with an improved deposition scheme and oceanic dispersion model, *Atmos. Chem. Phys.*, *15*(2), 1029-1070, doi:10.5194/acp-15-1029-2015.

Kitayama, K., et al. (2018), Atmospheric Modeling of ^{137}Cs Plumes From the Fukushima Daiichi Nuclear Power Plant-Evaluation of the Model Intercomparison Data of the Science Council of Japan, J. Geophys. Res.-Atmos., 123(14), 7754-7770, doi:10.1029/2017jd028230.

Li, J., Z. F. Wang, G. Zhuang, G. Luo, Y. Sun, and Q. Wang (2012), Mixing of Asian mineral dust with anthropogenic pollutants over East Asia: a model case study of a super-duststorm in March 2010, *Atmospheric Chemistry and Physic*, *12*(16), 7591-7607, doi:10.5194/acp-12-7591-2012.

Leadbetter, S. J., M. C. Hort, A. R. Jones, H. N. Webster, and R. R. Draxler (2015), Sensitivity of the modelled deposition of Caesium-137 from the Fukushima Dai-ichi nuclear power plant to the wet deposition parameterisation in NAME, *J. Environ. Radioact.*, *139*, 200-211, doi:10.1016/j.jenvrad.2014.03.018.

Liu, N., Ge, B., Fang, S. (2024). Supporting data for High-resolution convective wet scavenging simulations: A case study of the Fukushima Daiichi Nuclear Power Plant accident [Dataset]. Zenodo. https://doi.org/10.5281/zenodo.14504897.

Lu, Y., Z. Y. Guo, and J. P. Tang (2021), Research progress of convection permitting regional climate modeling, *Journal of the Meteorological Sciences (in Chinese)*, *41*(06), 818-827, doi:10.12306/2020jms.0010.

Mathieu, A., M. Kajino, I. Korsakissok, R. Périllat, D. Quélo, A. Quérel, O. Saunier, T. T. Sekiyama, Y. Igarashi, and D. Didier (2018), Fukushima Daiichi-derived radionuclides in the atmosphere, transport and deposition in Japan: A review, *Appl. Geochem.*, *91*, 122-139, doi:10.1016/j.apgeochem.2018.01.002.

Miyamoto, Y., K. Yasuda, and M. Magara (2014), Size distribution of radioactive particles collected at Tokai, Japan 6 days after the nuclear accident, *J. Environ. Radioact.*, *132*, 1-7, doi:10.1016/j.jenvrad.2014.01.010.

Mölders, N., and G. Kramm (2014), *Lectures in meteorology*, Springer Atmospheric Sciences.

Morino, Y., T. Ohara, M. Watanabe, S. Hayashi, and M. Nishizawa (2013), Episode Analysis of Deposition of Radiocesium from the Fukushima Daiichi Nuclear Power Plant Accident, *Environ. Sci. Technol.*, *47*(5), 2314-2322, doi:10.1021/es304620x.

Muramatsu, H., K. Kawasumi, T. Kondo, K. Matsuo, and S. Itoh (2015), Size-distribution of airborne radioactive particles from the Fukushima accident, *J. Radioanal. Nucl. Chem.*, *303*(2), 1459-1463, doi:10.1007/s10967-014-3690-0.

Nakajima, T., et al. (2017), Model depiction of the atmospheric flows of radioactive cesium emitted from the Fukushima Daiichi Nuclear Power Station accident, *Prog. Earth Planet. Sci.*, *4*, 18, doi:10.1186/s40645-017-0117-x.

Nenes, A., S. N. Pandis, and C. Pilinis (1998), ISORROPIA: A new thermodynamic equilibrium model for multiphase multicomponent inorganic aerosols, *Aquat. Geochem.*, *4*(1), 123-152, doi:10.1023/a:1009604003981.

NOAA (2024a), Integrated Surface Dataset (Global). [WWW Document] https://www.ncei.noaa.gov/access/search/dataset-search?text=Global%20hourly.

NOAA (2024b), NOAA Climate Data Record (CDR) of CPC Morphing Technique (CMORPH) High Resolution Global Precipitation Estimates, https://www.ncei.noaa.gov/products/climate-data-records/precipitation-cmorph

Odum, J. R., T. P. W. Jungkamp, R. J. Griffin, R. C. Flagan, and J. H. Seinfeld (1997), The atmospheric aerosol-forming potential of whole gasoline vapor, *Science*, *276*(5309), 96-99, doi:10.1126/science.276.5309.96.

Oura, Y., M. Ebihara, H. Tsuruta, T. Nakajima, T. Ohara, M. Ishimoto, H. Sawahata, Y. Katsumura, and W. Nitta (2015), A Database of Hourly Atmospheric Concentrations of Radiocesium (^{134}Cs and ^{137}Cs) in Suspended Particulate Matter Collected in March 2011 at 99 Air Pollution Monitoring Stations in Eastern Japan, *Journal of Nuclear and Radiochemical Sciences*, *15*(2), 2_1-2_12, doi:10.14494/jnrs.15.2_1.

Prein, A. F., et al. (2015), A review on regional convection-permitting climate modeling: Demonstrations, prospects, and challenges, *Rev. Geophys.*, *53*(2), 323-361, doi:10.1002/2014rg000475.

Roselle, S. J., and F. S. Binkowski (1999), Science algorithms of the EPA Models-3 Community multiscale air quality modeling system, Chapter 11: Cloud dynamics and chemistry.

Rossow, W. B., and C. Pearl (2007), 22-Year survey of tropical convection penetrating into the lower stratosphere, *Geophys. Res. Lett.*, *34*(4), 4, doi:10.1029/2006gl028635.

Saito, K., T. Shimbori, and R. Draxler (2015), JMA's regional atmospheric transport model calculations for the WMO technical task team on meteorological analyses for Fukushima Daiichi Nuclear Power Plant accident, *J. Environ. Radioact.*, *139*, 185-199, doi:10.1016/j.jenvrad.2014.02.007.

Sato, Y., et al. (2018), Model Intercomparison of Atmospheric ^{137}Cs From the Fukushima Daiichi Nuclear Power Plant Accident: Simulations Based on Identical Input Data, *J. Geophys. Res.-Atmos.*, *123*(20), 11748-11765, doi:10.1029/2018jd029144.

Skamarock, W. C., J. Klemp, J. Dudhia, D. Gill, Z. Liu, J. Berner, W. Wang, J. Powers, M. Duda, and D. Barker (2019), A description of the advanced research WRF model version 4 (Vol. 145), *J National Center for Atmospheric Research*.

Tan, Q. X., et al. (2023), Unexpected high contribution of in-cloud wet scavenging to nitrogen deposition induced by pumping effect of typhoon landfall in China, *Environ. Res. Commun.*, *5*(2), 12, doi:10.1088/2515-7620/acb90b.

Tsuruta, H., Y. Oura, M. Ebihara, T. Ohara, and T. Nakajima (2014), First retrieval of hourly atmospheric radionuclides just after the Fukushima accident by analyzing filter-tapes of operational air pollution monitoring stations, *Sci Rep*, *4*, 10, doi:10.1038/srep06717.

Walcek, C. J., and N. M. Aleksic (1998), A simple but accurate mass conservative, peak-preserving, mixing ratio bounded advection algorithm with Fortran code, *Atmos. Environ.*, *32*(22), 3863-3880, doi:10.1016/s1352-2310(98)00099-5.

Wang, Y., W. W. Xia, and G. J. Zhang (2021), What rainfall rates are most important to wet removal of different aerosol types?, *Atmos. Chem. Phys.*, *21*(22), 16797-16816, doi:10.5194/acp-21-16797-2021.

Wang, Z. F., T. Maeda, M. Hayashi, L. F. Hsiao, and K. Y. Liu (2001), A nested air quality prediction modeling system for urban and regional scales: Application for high-ozone episode in Taiwan, *Water Air Soil Pollut.*, *130*(1-4), 391-396, doi:10.1023/a:1013833217916.

Weisman, M. L., W. C. Skamarock, and J. B. Klemp (1997), The resolution dependence of explicitly modeled convective systems, *Mon. Weather Rev.*, *125*(4), 527-548, doi:10.1175/1520-0493(1997)125<0527:Trdoem>2.0.Co;2.

Wesely, M. L. (1989), Parameterization of surface resistances to gaseous dry deposition in regional-scale numerical-models, *Atmos. Environ.*, *23*(6), 1293-1304, doi:10.1016/0004-6981(89)90153-4.

Wu, D., J. Tian, T. Hu, and N. Fu (2023), Sensitivity Study of Cumulus Convective Parameterization at a Gray Zone during a Heavy Precipitation Process over the Northeastern Tibetan Plateau, *Chinese Journal of Atmospheric Sciences*, *47*(4), 1247-1266.

Xia, W. W., Y. Wang, G. J. Zhang, Z. Y. Cui, B. Wang, Y. J. He, and X. Wang (2022), Unexpected Changes of Aerosol Burdens With Decreased Convection in the Context of Scale-Aware Convection Schemes, *Geophys. Res. Lett.*, *49*(11), 10, doi:10.1029/2022gl099008.

Xu, D. H. (2020), The study of below-cloud wet scavenging mechanism for aerosols and its numerical simulation (in Chinese), 146 pp, Institute of Atmospheric Physics, Chinese Academy of Sciences, Beijing.

Xu, D. H., B. Z. Ge, X. S. Chen, Y. L. Sun, N. L. Cheng, M. Li, X. L. Pan, Z. Q. Ma, Y. P. Pan, and Z. F. Wang (2019), Multi-method determination of the below-cloud wet scavenging coefficients of aerosols in Beijing, China, *Atmos. Chem. Phys.*, *19*(24), 15569-15581, doi:10.5194/acp-19-15569-2019.

Yang, Q., et al. (2015), Aerosol transport and wet scavenging in deep convective clouds: A case study and model evaluation using a multiple passive tracer analysis approach, *J. Geophys. Res.-Atmos.*, *120*(16), 8448-8468, doi:10.1002/2015jd023647.

Yu, H. Y., P. X. Li, and K. C. Wang (2025), A review on convection-permitting modeling of extreme precipitation (in Chinese), *Chinese Science bulletin*, 1-16, doi:10.1360/TB-2024-1061.

Zaveri, R. A., and L. K. Peters (1999), A new lumped structure photochemical mechanism for large-scale applications, *J. Geophys. Res.-Atmos.*, *104*(D23), 30387-30415, doi:10.1029/1999jd900876.

Zhang, L. M., J. R. Brook, and R. Vet (2003), A revised parameterization for gaseous dry deposition in air-quality models, *Atmos. Chem. Phys.*, *3*, 2067-2082, doi:10.5194/acp-3-2067-2003.

Zhang, L. M., S. L. Gong, J. Padro, and L. Barrie (2001), A size-segregated particle dry deposition scheme for an atmospheric aerosol module, *Atmos. Environ.*, *35*(3), 549-560, doi:10.1016/s1352-2310(00)00326-5.

Zhang, Y. Q., J. K. Roundy, and J. A. Santanello (2021), Evaluating the impact of model resolutions and cumulus parameterization on precipitation in NU-WRF: A case study in the Central Great Plains, *Environ. Modell. Softw.*, *145*, 12, doi:10.1016/j.envsoft.2021.105184.

Zhao, J. Y., J. K. Tan, S. Chen, Q. Q. Huang, L. Gao, Y. P. Li, and C. X. Wei (2024), Intelligent Reconstruction of Radar Composite Reflectivity Based on Satellite

Observations and Deep Learning, *Remote Sens.*, *16*(2), 19, doi:10.3390/rs16020275.

Zhuang, S. H., S. Fang, D. Goto, X. W. Dong, Y. H. Xu, and L. Sheng (2023), Model behavior regarding in- and below-cloud ^{137}Cs wet scavenging following the Fukushima accident using 1-km-resolution meteorological field data, *Sci. Total Environ.*, *872*, 12, doi:10.1016/j.scitotenv.2023.162165.

Zhuang, S. H., S. Fang, Y. H. Xu, D. Goto, and X. W. Dong (2024), Wet scavenging of multi-mode ^{137}Cs aerosols following the Fukushima accident: Size-resolved microphysics modeling with observed diameters, *Sci. Total Environ.*, *917*, 13, doi:10.1016/j.scitotenv.2024.170287.

Figure 1.

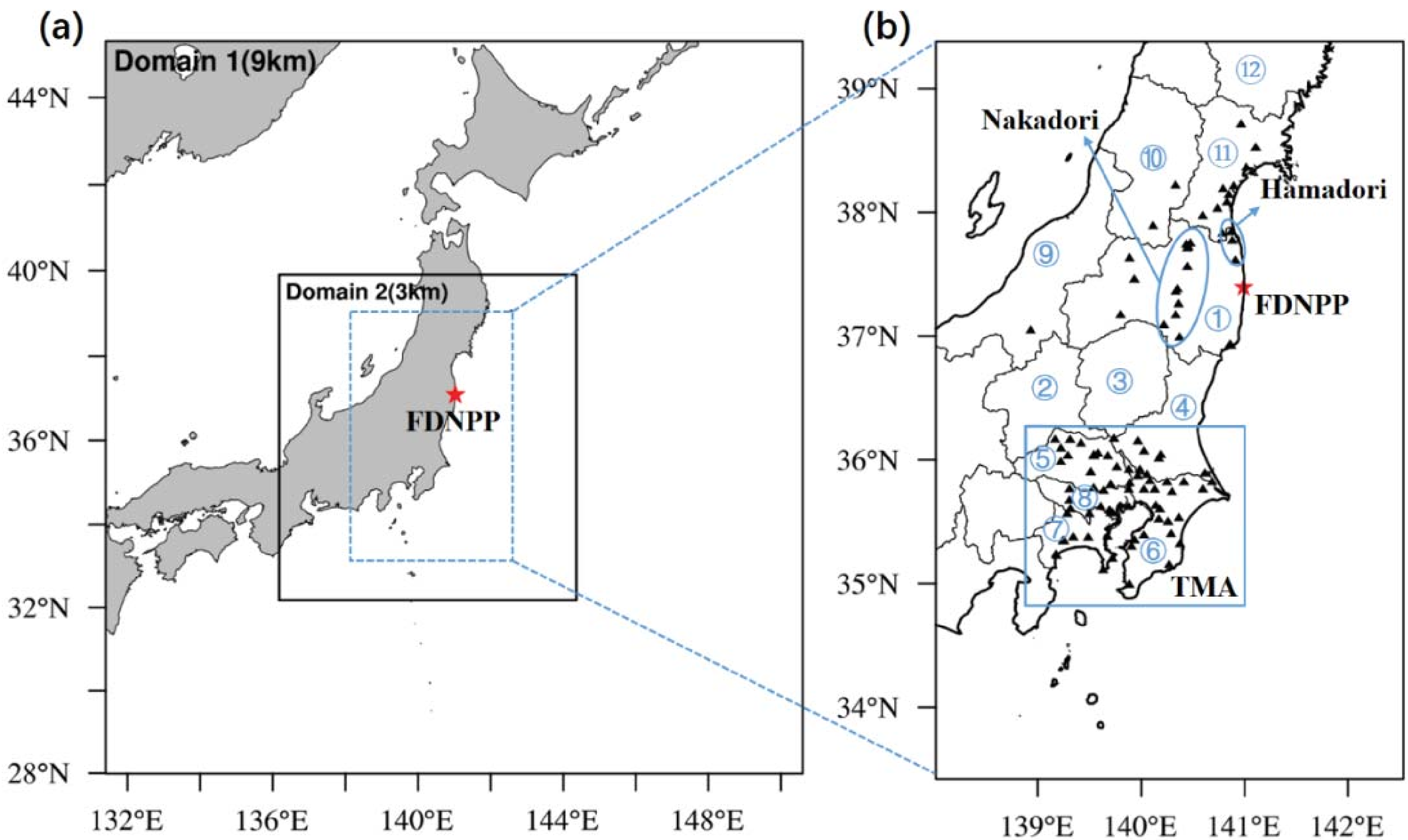

(a)
Domain 1(9km)
Domain 2(3km)
FDNPP
44°N
40°N
36°N
32°N
28°N
132°E
136°E
140°E
144°E
148°E
(b)
Nakadori
Hamadori
FDNPP
TMA
①
②
③
④
⑤
⑥
⑦
⑧
⑨
⑩
⑪
⑫
39°N
38°N
37°N
36°N
35°N
34°N
139°E
140°E
141°E
142°E

Figure 2.

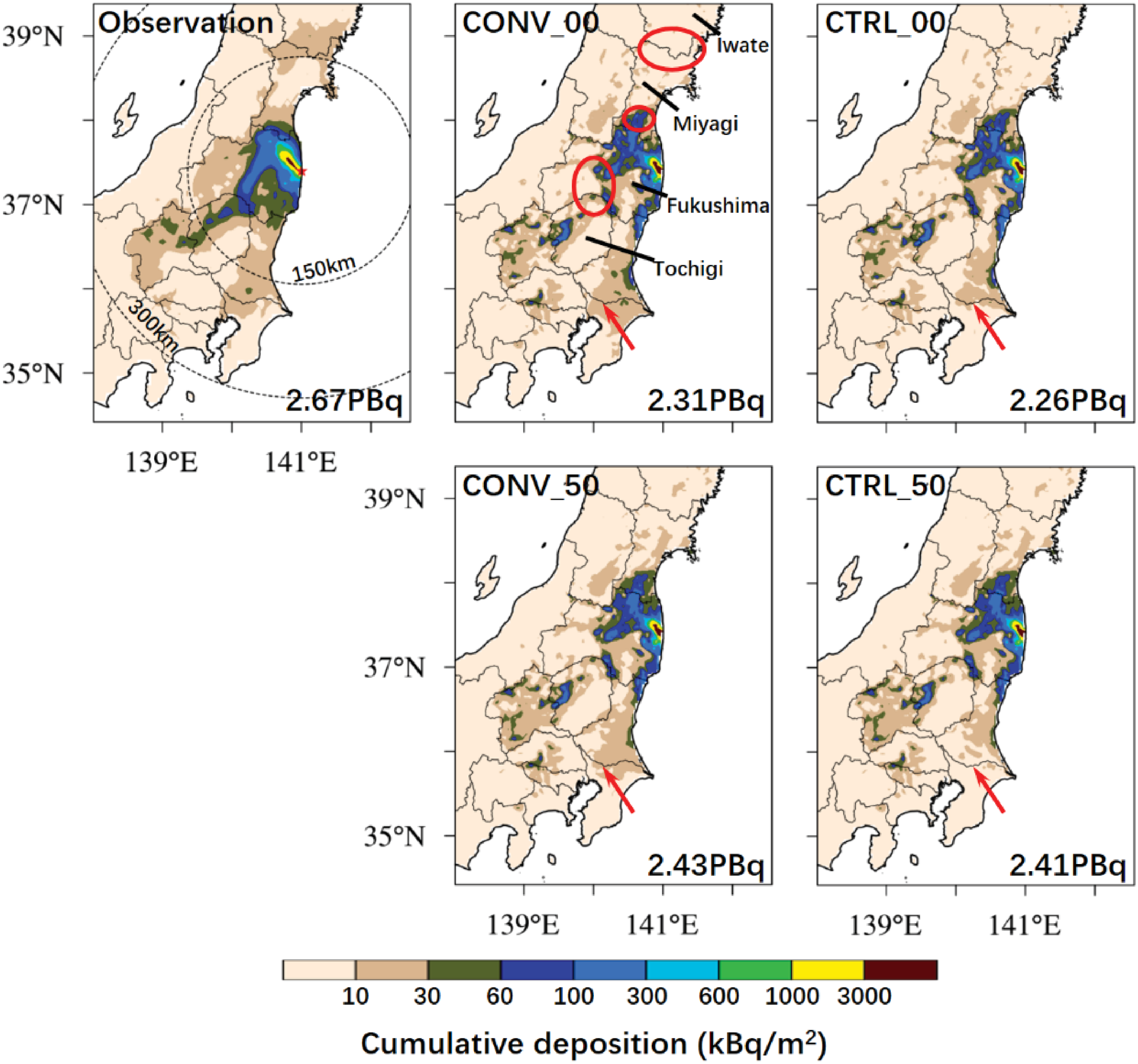
Observation
CONV_00
CTRL_00
CONV_50
CTRL_50
Iwate
Miyagi
Fukushima
Tochigi
150km
300km
2.67PBq
2.31PBq
2.26PBq
2.43PBq
2.41PBq
39°N
37°N
35°N
139°E
141°E
10
30
60
100
300
600
1000
3000
Cumulative deposition (kBq/m²)

Figure 3.

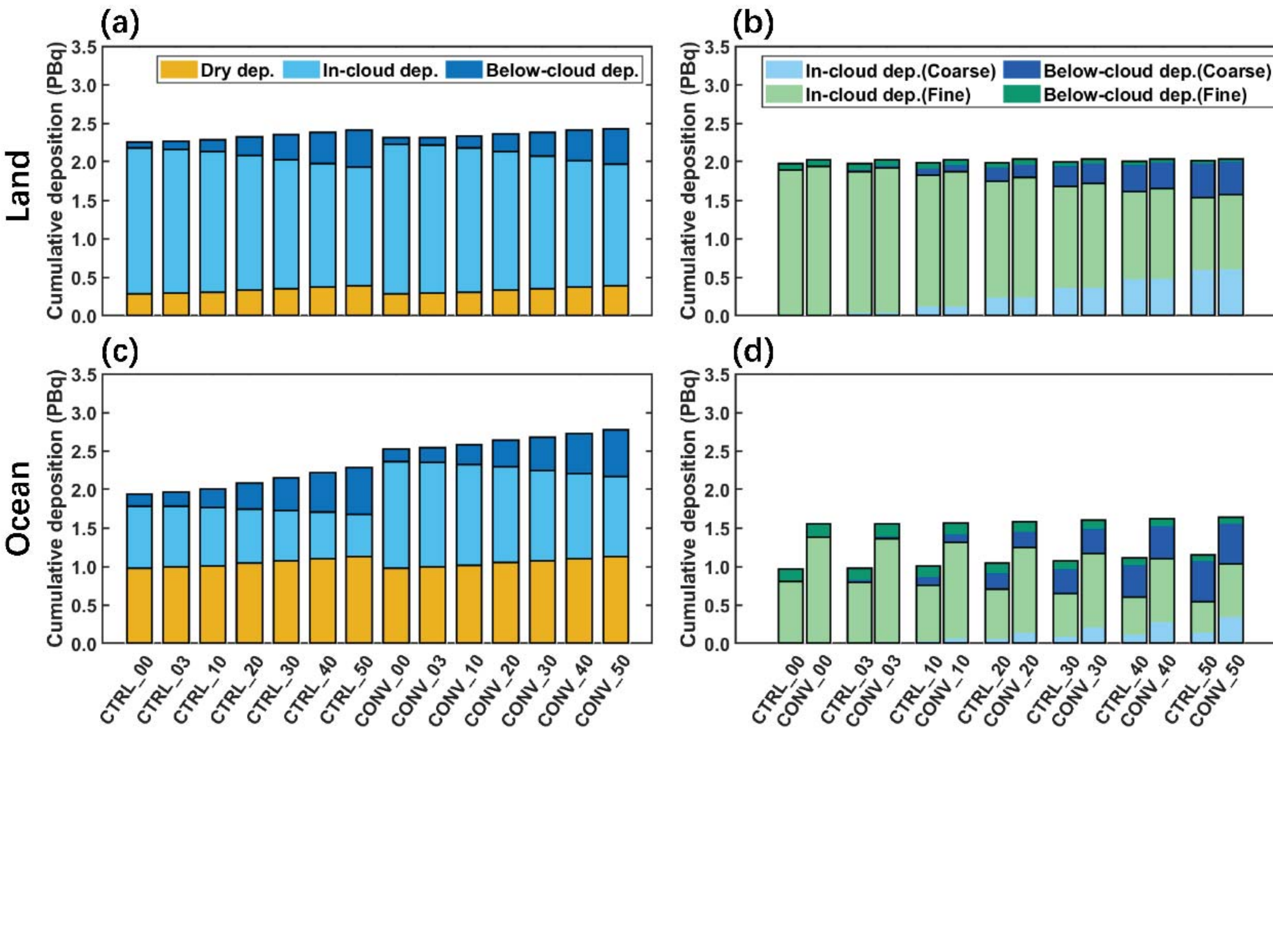

(a)
(b)
(c)
(d)
Land
Ocean
Cumulative deposition (PBq)
Dry dep.
In-cloud dep.
Below-cloud dep.
In-cloud dep.(Coarse)
Below-cloud dep.(Coarse)
In-cloud dep.(Fine)
Below-cloud dep.(Fine)
CTRL_00
CTRL_03
CTRL_10
CTRL_20
CTRL_30
CTRL_40
CTRL_50
CONV_00
CONV_03
CONV_10
CONV_20
CONV_30
CONV_40
CONV_50

Figure 4.

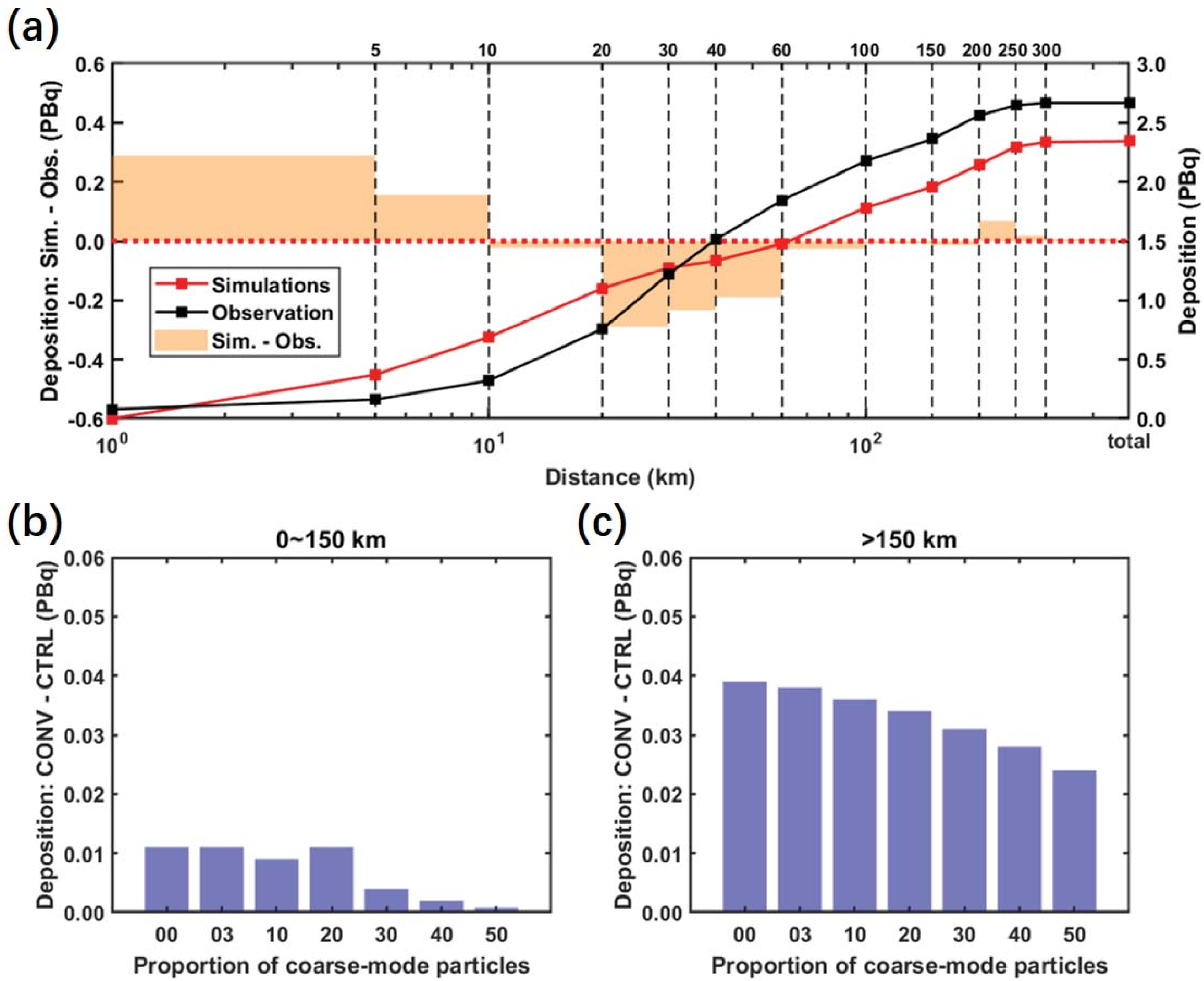

(a)
5
10
20
30
40
60
100
150
200
250
300
Simulations
Observation
Sim. - Obs.
Deposition: Sim. - Obs. (PBq)
Deposition (PBq)
total
Distance (km)
(b)
0~150 km
Deposition: CONV - CTRL (PBq)
Proportion of coarse-mode particles
(c)
>150 km
Deposition: CONV - CTRL (PBq)
Proportion of coarse-mode particles

Figure 5.

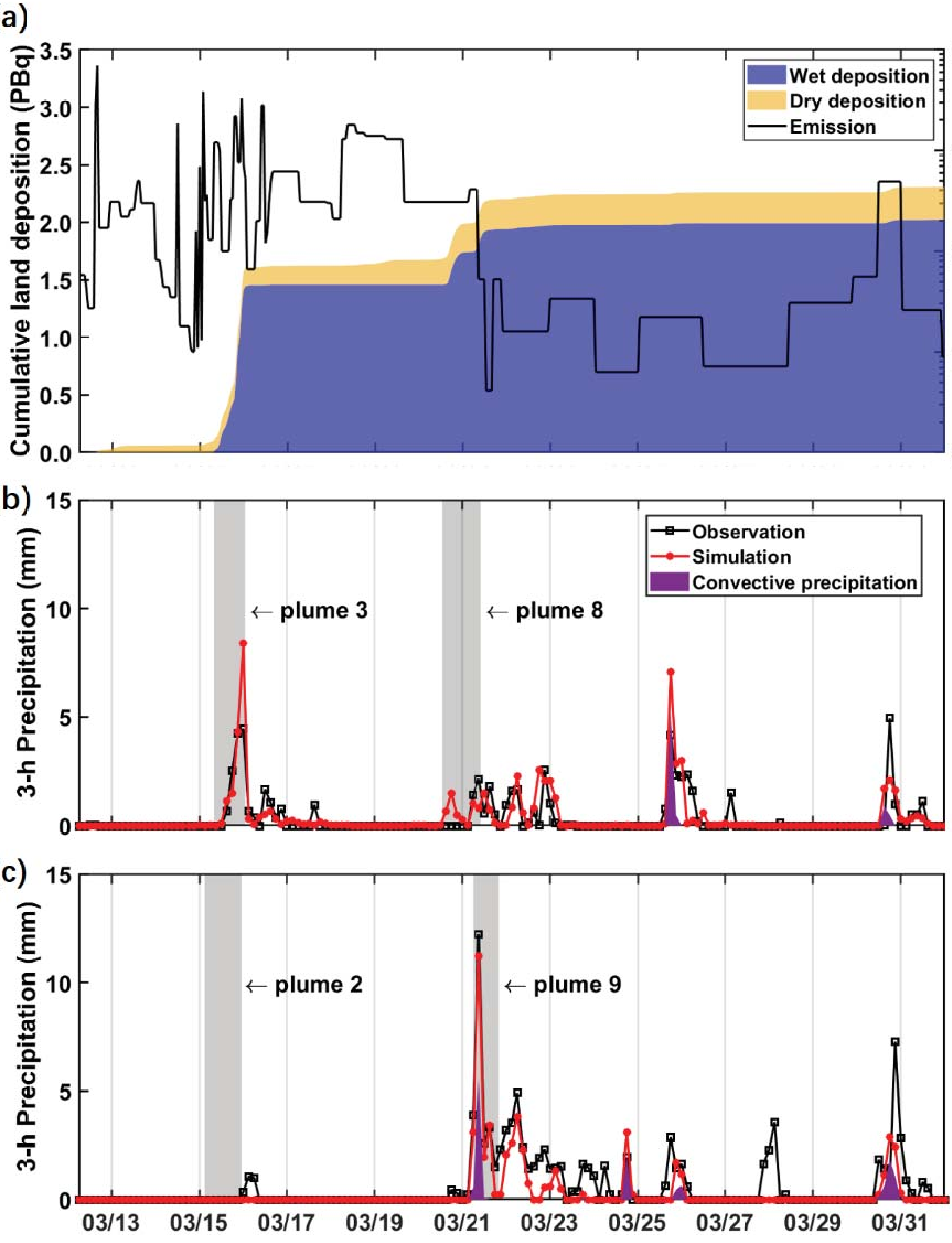
(a)
Cumulative land deposition (PBq)
3.5
3.0
2.5
2.0
1.5
1.0
0.5
0.0
Emission rate (TBq h-1)
Wet deposition
Dry deposition
Emission
(b)
3-h Precipitation (mm)
15
10
5
0
Observation
Simulation
Convective precipitation
← plume 3
← plume 8
(c)
← plume 2
← plume 9
03/13
03/15
03/17
03/19
03/21
03/23
03/25
03/27
03/29
03/31

Figure 6.

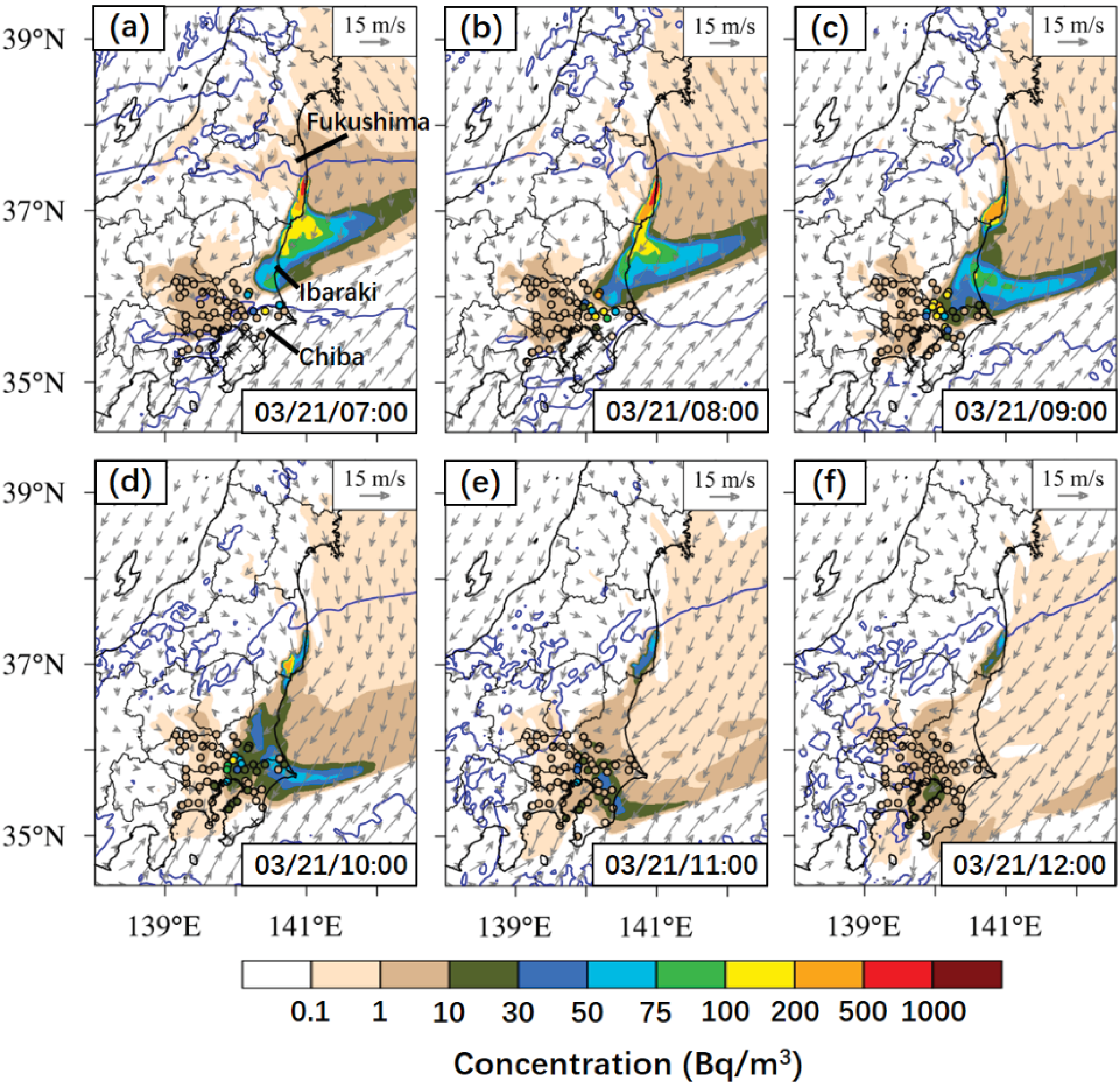

(a)
(b)
(c)
(d)
(e)
(f)
15 m/s
Fukushima
Ibaraki
Chiba
03/21/07:00
03/21/08:00
03/21/09:00
03/21/10:00
03/21/11:00
03/21/12:00
39°N
37°N
35°N
139°E
141°E
0.1
1
10
30
50
75
100
200
500
1000
Concentration (Bq/m³)

Figure 7.

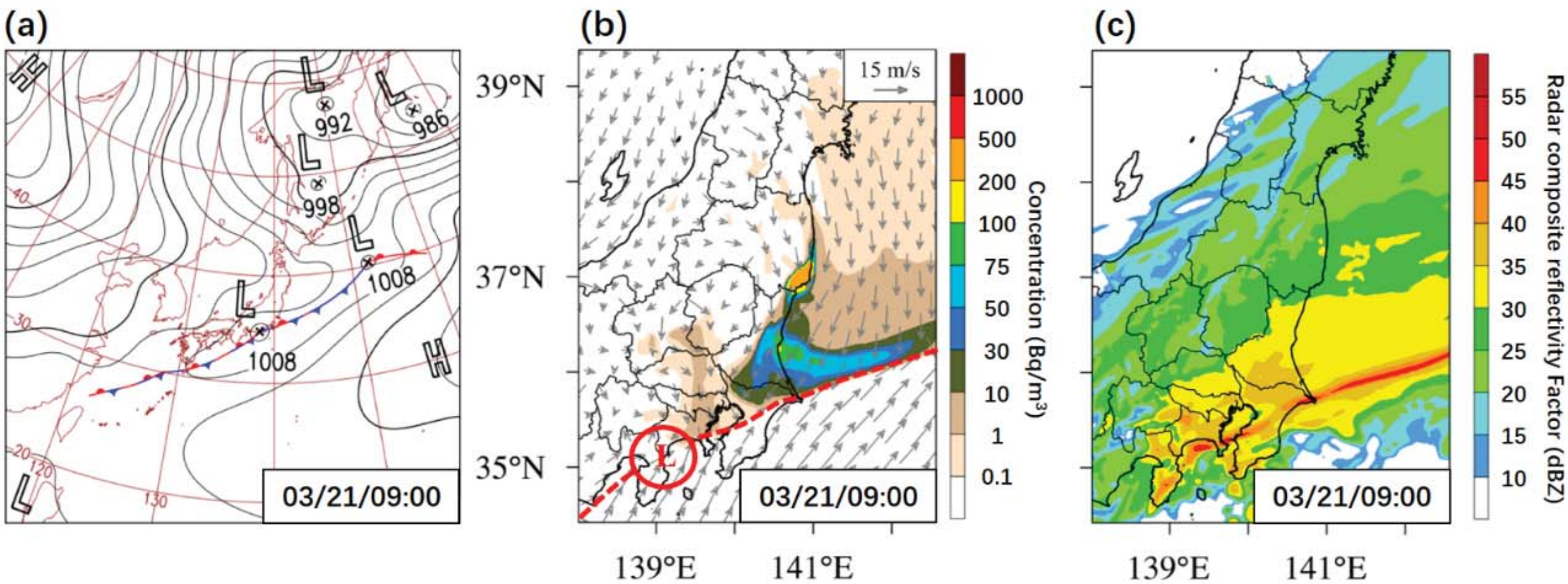
(a)
986
992
998
1008
1008
40
30
20
120
130
03/21/09:00
(b)
15 m/s
39°N
37°N
35°N
139°E
141°E
03/21/09:00
1000
500
200
100
75
50
30
10
1
0.1
Concentration (Bq/m^3)
(c)
139°E
141°E
03/21/09:00
55
50
45
40
35
30
25
20
15
10
Radar composite reflectivity Factor (dBZ)

Figure 8.

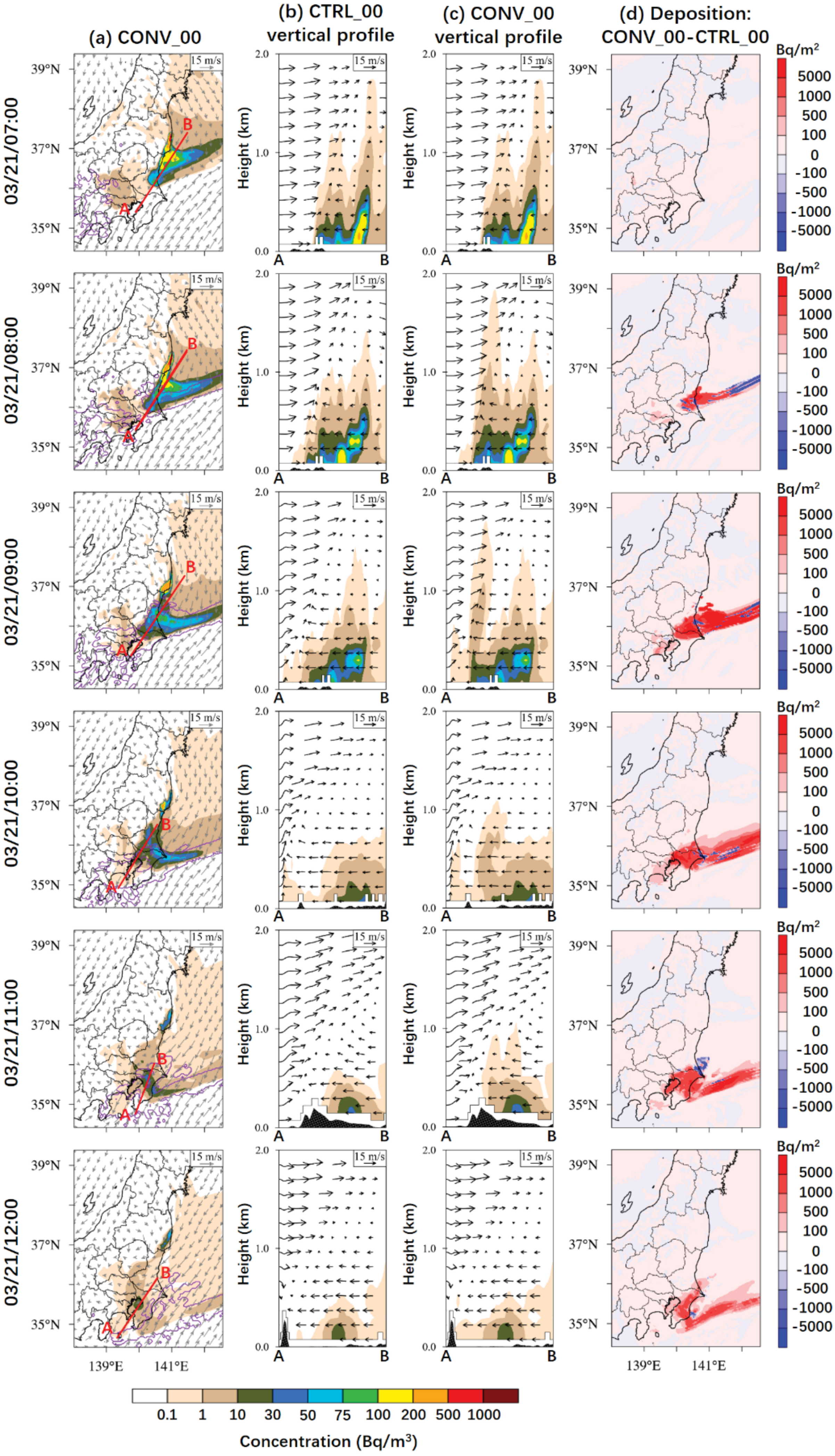
(a) CONV_00
(b) CTRL_00 vertical profile
(c) CONV_00 vertical profile
(d) Deposition: CONV_00-CTRL_00
03/21/07:00
03/21/08:00
03/21/09:00
03/21/10:00
03/21/11:00
03/21/12:00
39°N
37°N
35°N
139°E
141°E
15 m/s
Height (km)
A
B
Bq/m²
5000
1000
500
100
0
-100
-500
-1000
-5000
0.1
1
10
30
50
75
100
200
500
1000
Concentration (Bq/m³)

Figure 9.

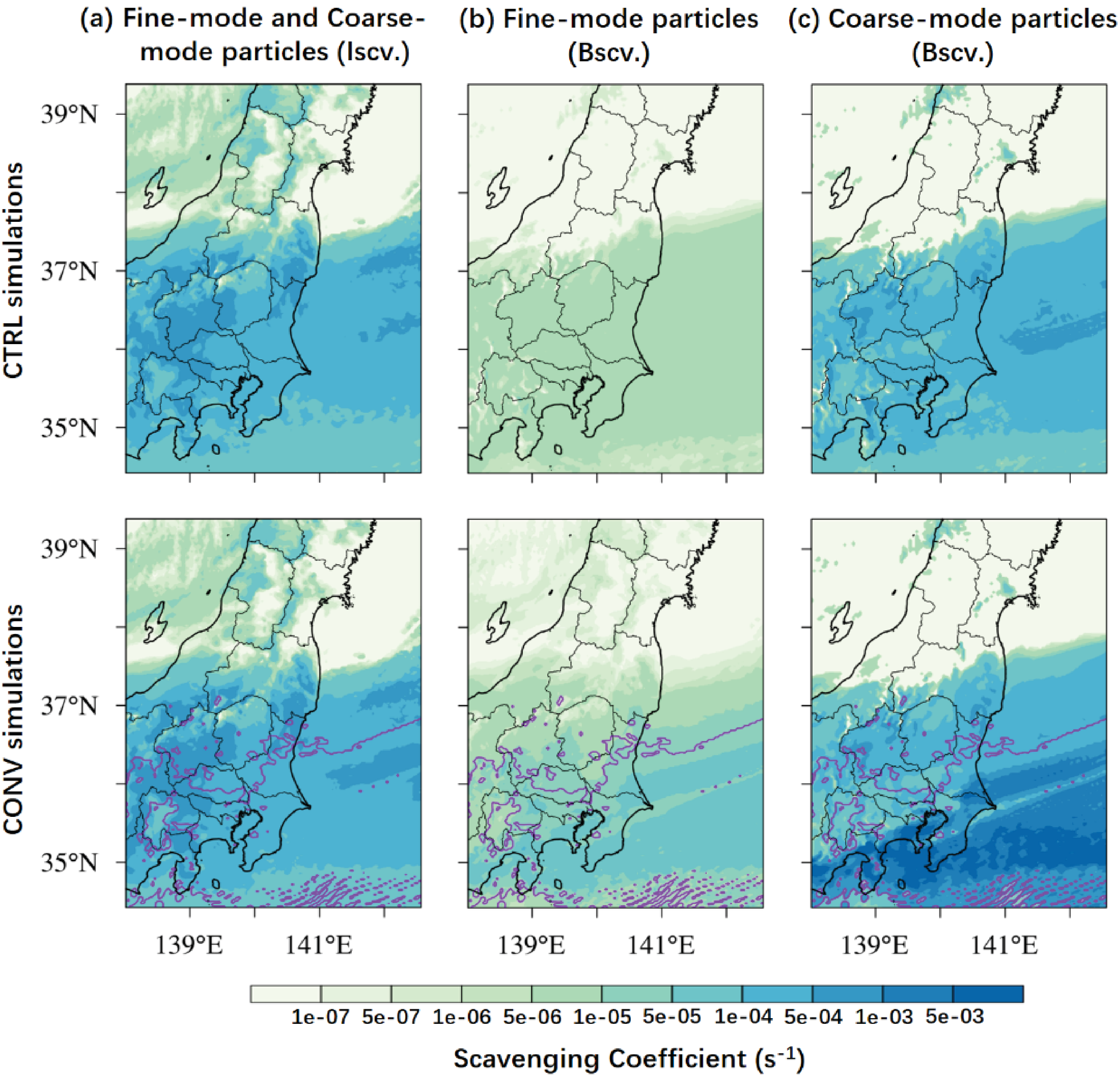

(a) Fine-mode and Coarse-mode particles (Iscv.)
(b) Fine-mode particles (Bscv.)
(c) Coarse-mode particles (Bscv.)
CTRL simulations
CONV simulations
39°N
37°N
35°N
139°E
141°E
1e-07
5e-07
1e-06
5e-06
1e-05
5e-05
1e-04
5e-04
1e-03
5e-03
Scavenging Coefficient (s-1)

Figure 10.

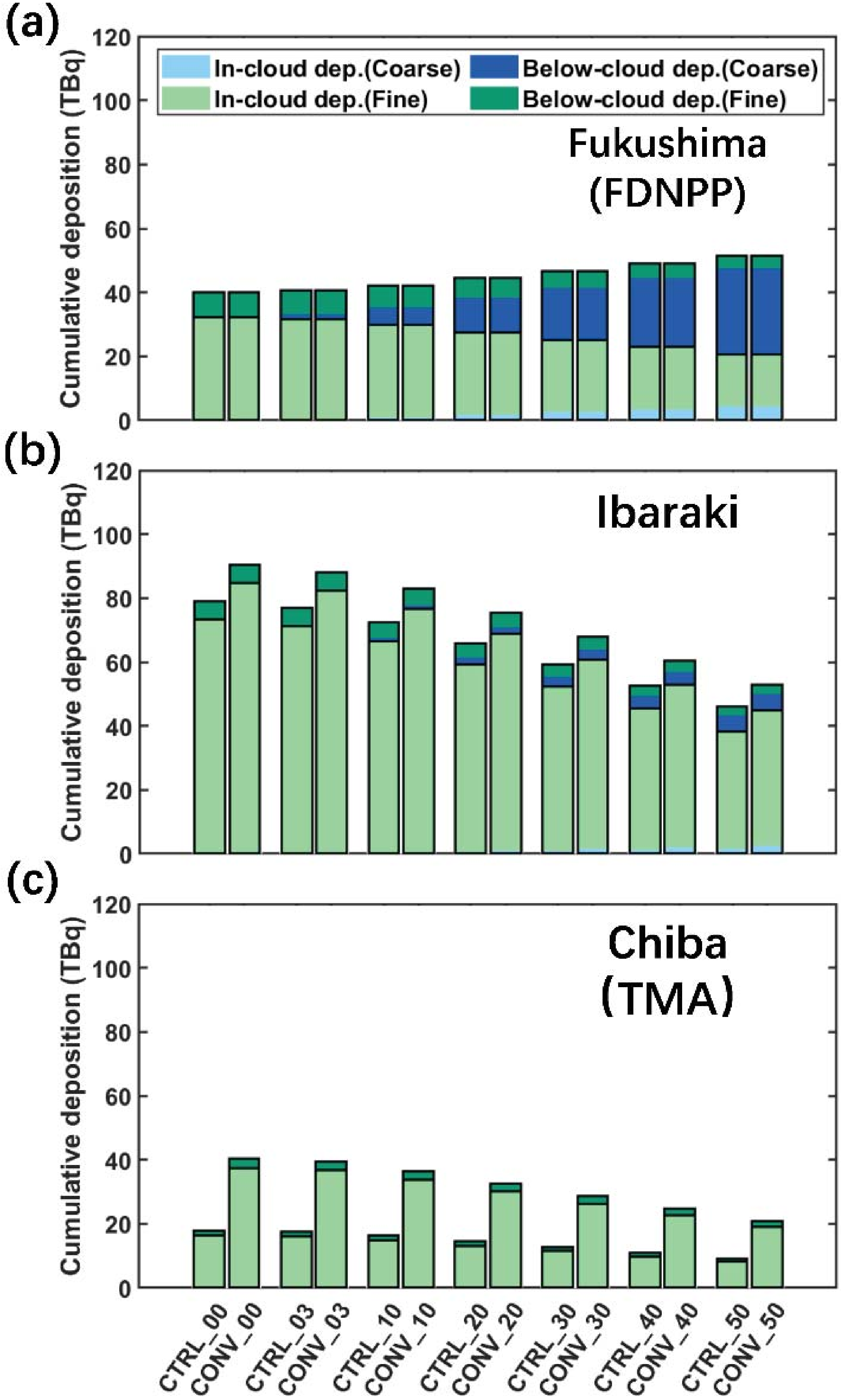
(a)
(b)
(c)
Cumulative deposition (TBq)
In-cloud dep.(Coarse)
Below-cloud dep.(Coarse)
In-cloud dep.(Fine)
Below-cloud dep.(Fine)
Fukushima
(FDNPP)
Ibaraki
Chiba
(TMA)
0
20
40
60
80
100
120
CTRL_00
CONV_00
CTRL_03
CONV_03
CTRL_10
CONV_10
CTRL_20
CONV_20
CTRL_30
CONV_30
CTRL_40
CONV_40
CTRL_50
CONV_50